PHYSICAL REVIEW FLUIDS **7**, 034202 (2022)

Diffusiophoresis in a Taylor-dispersing solute

Robben E. Migacz and Jesse T. Ault[*]
Center for Fluid Mechanics, School of Engineering, Brown University, Providence, Rhode Island 02912, USA

(Received 3 September 2021; accepted 16 February 2022; published 7 March 2022;
corrected 6 July 2022)

We consider the diffusiophoresis of a suspension of charged colloidal particles in the presence of a nonuniform solute concentration, where each species experiences Taylor dispersion from spanwise velocity gradients. We describe the two-dimensional evolution of both solute and particle concentration fields in a narrow channel with background Poiseuille flow by applying the lubrication approximation along with the assumption of constant particle ζ potential. We compare the theoretical predictions with the results of numerical simulations for fixed particle ζ potential, demonstrating good agreement. Finally, we comment on three-dimensional effects, long-time dynamics, and the validity of the constant particle ζ potential assumption for our model. We perform additional simulations with a simple variable-ζ potential model that treats the particle ζ potential as a logarithmic function of solute concentration. The results show good qualitative and quantitative agreement, supporting the use of the constant particle ζ potential assumption for this system under certain circumstances.

DOI: 10.1103/PhysRevFluids.7.034202

I. INTRODUCTION

Flows containing both dissolved solute molecules and dispersed colloidal particles are common in filtrations, microfluidic devices, and laboratory-on-a-chip sensors. Often, such flows occur in narrow channels, such as blood vessels or medical tubing. An understanding of solute–particle interactions and the dynamics of each species in a flow is critical for the design and evaluation of such systems, and analytical models for such dynamics can reduce computational effort and development time relative to direct numerical simulation or provide insight into observed behaviors. There are multiple timescales in practical applications of diffusiophoresis, owing to fluid velocity and differences in solute and particle diffusivity. We describe how two-dimensional features that develop in particle concentration profiles on short timescales can persist on much longer timescales by considering the early-time dynamics of diffusiophoresis in a narrow channel.

The motion of particles in flows with solute gradients is the result of bulk fluid motion, diffusion, and diffusiophoresis, which arises due to interactions between the particles and solute molecules. Diffusion is enhanced by shear stresses in the flow; velocity gradients cause nonuniform solute transport, which leads to cross-stream solute gradients [1]. The diffusiophoretic motion is the result of interactions between solute molecules and the colloidal particles and consists of contributions due to both electrophoresis and chemiphoresis [2]. Its direction is dependent on the gradient of solute concentration and the species present in the flow [3]. The diffusiophoretic velocity is proportional to the gradient of the logarithm of solute concentration, and the proportionality constant, known as the diffusiophoretic mobility, varies with the ζ potential of the particles [3].

The earliest descriptions of diffusiophoresis were provided by Derjaguin *et al.* [4,5], who modeled particle velocities and described diffusioosmotic flows resulting from solute gradients near

---

[*] jesse_ault@brown.edu

solid surfaces. Many studies have explored diffusiophoresis and its applications in recent decades, reflecting an increased interest in the dynamics of particles in the presence of nonuniform solute concentrations. Such works may have direct applications in industry, medicine, or biology, or they might provide the means for measuring physical properties of the species in a flow. Anderson [6] described diffusiophoresis and commented on an apparent lack of appreciation for the phenomenon; early works demonstrated diffusiophoresis and described experimental measurements of particle dynamics [7–9], but applications were limited. Since then, numerous studies have provided context and applications for diffusiophoretic flows. Shin *et al.* [10], for example, performed microfluidic experiments and numerical simulations to study the dynamics of colloidal particles in junctions between flows. Particles were packed into pores and their aggregation caused irreversible clogging. Such interactions have significant implications for the design and maintenance of medical and industrial equipment. Other works have also examined diffusiophoresis and diffusioosmosis as a mechanism for particle transport in porous media [11,12]. Shin *et al.* [3] also considered colloid transport in dead-end channels, commenting that the transport of particles to or from channels is inefficient when dependent on stochastic processes alone. They employed diffusiophoresis to effectively enhance particle transport. Shim and Stone [13] described the aggregation of charged particles in channel flows with CO_2 leakage through gas-permeable walls, and Shim *et al.* [14] have recently used diffusiophoresis driven by CO_2 to prevent the aggregation of bacteria near interfaces and potentially inhibit the formation of biofilms. Similarly, Florea *et al.* [15] commented on the development of an exclusion zone caused by the diffusiophoretic migration of particles, with potential applications in filtrations and separations [16]. Recently, Lee *et al.* [17] examined diffusiophoresis with a pseudospectral method and commented on the effects of parameters like the surface charge density and electrolyte strength.

Other studies focus on modeling diffusiophoresis, either to provide descriptions of solute and particle dynamics or to suggest novel techniques to measure electrical or chemical properties. Raynal *et al.* [18], for example, studied the dispersion of solute and particles in linear velocity fields. Ault *et al.* [19] studied the diffusiophoretic motion of colloidal particles, assuming solute gradients are one-dimensional. They provided theoretical descriptions of particle dynamics to inform techniques for controlled particle injection or removal. Chu *et al.* [20] modeled one-dimensional advective–diffusive particle spreading via diffusiophoresis. More recently, they considered the long-time behavior—after spanwise variations in concentration have diminished—of colloidal species undergoing diffusiophoresis in a channel flow under the influence of Taylor dispersion [21]. They provided a macrotransport equation and numerical results for comparison, demonstrating agreement and commenting on the relatively low computational effort needed to calculate the long-time dynamics. Ault *et al.* [22] found analytical expressions for the dynamics of solute and particles in long, narrow channels, focusing on quasi-one-dimensional dynamics and providing leading-order corrections for two-dimensional diffusioosmotic effects. They commented on potential applications in particle sorting and ζ potentiometry. Ault *et al.* [23] later applied diffusiophoresis to measure either ζ potentials or interaction length scales for surfaces exposed to electrolyte or nonelectrolyte solutes, respectively. They gave analytical solutions for each, allowing microfluidic experiments to be used for the measurement of parameters. Similarly, Rasmussen *et al.* [24] used diffusiophoresis and diffusioosmosis to measure the ζ potential and size of nanoparticles with applications in medical diagnostics, while Shi *et al.* [25] introduced steady-state gradients of solute and commented on applications in measuring diffusiophoretic mobility. Alessio *et al.* [26] recently described diffusiophoresis in two-dimensional pores with gradients of multiple electrolytes. There are numerous other potential applications of diffusiophoresis; Velegol *et al.* [27] listed sources of solute concentration gradients, including chemical reactions, sedimentation, and evaporation, and various situations where diffusiophoresis could be applied or studied.

Other works describe the two-dimensional dynamics of species in channel flows, which is a cornerstone of the present work. Taylor dispersion, the enhanced effective diffusion of a substance in the presence of a background shear flow, has been previously studied by numerous researchers. Taylor [1] first provided a description of the enhancement of diffusion in shear flows, which was later generalized by Aris [28]. Shear stresses in the flow in a channel change the direction of concentration gradients, resulting in cross-stream diffusion and, ultimately, enhanced diffusion in the streamwise direction. Descriptions of this phenomenon have been improved and extended with time; other works, such as those by Frankel and Brenner [29] and Barton [30], have given mathematically rigorous descriptions of dispersion phenomena. More recent works have continued to extend earlier results to novel applications; Chu *et al.* [31], for instance, studied the dynamics of solute in a narrow channel with an oscillatory velocity, developing a generalized Taylor dispersion theory. Taylor dispersion is particularly relevant to channel flows and has been considered in the context of diffusiophoresis. Specifically, recent work by Chu *et al.* [21] considered the addition of charged colloidal particles to such a system in which a solute concentration field experiences Taylor dispersion, and they considered the long-time (approximately one-dimensional) behavior of their coupled dynamics via diffusiophoresis. At such times, variations in concentration across the channel can be neglected [32]. Here, we perform a theoretical and numerical modeling of the early-time coupled dynamics in a channel flow, which has not previously been explored. While previous work by Chu *et al.* [31] focused on the quasi-one-dimensional and long-time dynamics and recent work by Raynal *et al.* [18] considered dynamics in linear velocity fields, to the best of our knowledge there are no descriptions of the coupled solute and particle dynamics in channel flows at early times. Furthermore, a key feature and motivation behind this work that we will show is that the "early-time" dynamics can in fact persist significantly longer than might be expected.

For a physical system such as this, there are multiple important timescales of interest. In general, these are the characteristic times of fluid advection both along and across the channel (L/U and h/U), the particle and solute diffusion both along and across the channel (h^2/D_s, L^2/D_s, h^2/D_p, and L^2/D_p), and the particle diffusiophoresis both along and across the channel (h^2/Γ_p and L^2/Γ_p). Here, L is the channel length, h is the channel width, U is the mean flow velocity in the channel, D_s is the solute diffusivity, D_p is the particle diffusivity, and Γ_p is the particle diffusiophoretic mobility. To characterize the dynamics of such a system, it is valuable to understand the relative magnitudes of the different timescales. In particular, since diffusiophoresis is coupled to the solute diffusion, it is typically reasonable to assume that $\Gamma_p \sim \mathcal{O}(D_s)$. Furthermore, depending on the size of the colloidal particles, it should typically be the case that $D_p < D_s$, and in fact we often have $D_p \ll D_s$. For example, with NaCl as the solute and particles with radius 100 nm, we have $D_s = 1.61 \times 10^{-9}\,\mathrm{m^2\,s^{-1}}$ and $D_p \approx 2.45 \times 10^{-12}\,\mathrm{m^2\,s^{-1}}$, such that $D_p/D_s = \mathcal{O}(10^{-3})$. This leads us to consider the "early" and "late" time dynamics for the system. In the context of the recent work [21], we consider the late time dynamics to be reached over the timescale h^2/D_p. Over this timescale, the particle concentration smooths out across the channel, and the quasi-1D model by Chu *et al.* [21] successfully describes the dynamics.

Thus, in the current work, we consider the early-time regime to be that before $t \sim \mathcal{O}(h^2/D_p)$, where we must still account for spatial variations in particle concentration across the channel. Before proceeding with the following analysis, we must first consider whether such a time regime is relevant to any real physical systems. As mentioned, if we consider particles with radius 100 nm, and typical microfluidic channels on the order of $h = 10$ to $100\,\mu\mathrm{m}$, we find that the early-time regime can potentially last from $t = \mathcal{O}(10\,\mathrm{s})$ up to $\mathcal{O}(1000\,\mathrm{s})$. For colloidal particles on the order of one micron or larger, the early-time regime will persist even longer. Thus, a general guideline for considering the dynamics in such a system is that when the typical time of the experiment is on the order of h^2/D_p or larger, the long-time quasi-1D solution of [21] will reasonably approximate the dynamics. For all shorter time periods, the spatial variation in particle and solute concentrations across the channel needs to be accounted for, as will be shown in our theoretical descriptions.

Here, we provide a description of these early-time dynamics—at times t on the order of h^2/D_s, where h^2 is the channel height and D_s is the solute diffusivity—of solute molecules and dispersed colloidal particles with both numerical solutions and analytical models. Our model applies for D_p both on the order of D_s as well as when it is much smaller. As mentioned, we assume the diffusiophoretic mobility Γ_p is on the order of D_s. For a *typical* case of interest (e.g., NaCl solute and 100 nm particles), the timescale for diffusion of solute across the channel is small relative to that of the particles because of the contrast between D_s and the particle diffusivity D_p. With (species-dependent) diffusivity values estimated in Sec. V, the difference between diffusive timescales for solute and particles is on the order of 10^3. We expect, therefore, that two-dimensional variations in particle concentration that develop in the early-time regime will persist for an extended time. That is to say that solute concentration profile will evolve and smooth out across the channel over the relatively fast timescale h^2/D_s, driving the particles toward or away from the channel walls via diffusiophoresis. Even though the driving force for cross-stream diffusiophoresis decays over this relatively fast timescale, the spatial variation in the particle concentration across the cross-section will persist for much longer [i.e., until $t \sim \mathcal{O}(h^2/D_p)$]; we demonstrate this in Appendix C.

To study the early-time dynamics, we apply the lubrication approximation [33] to develop solutions as series expanded about the aspect ratio of the channel. We briefly comment on the applicability of a two-dimensional model in a laboratory setting and later extend the analysis to consider the long-time dynamics. Our analytical solutions assume the ζ potential of the particles is constant, which is generally a reasonable assumption with symmetric electrolytes when the background solute concentration is low and the solute concentration gradients are not too large [34]. While numerous works assume the particle ζ potential or diffusiophoretic mobility are constant [10,19,23,35], in reality the ζ potential is affected by concentration, pH, and temperature, among other factors [34]. A parallel work by Lee *et al.* [36] demonstrates that the constant-ζ potential assumption can fail to capture all relevant dynamics of diffusiophoretic and diffusioosmotic transport in various contexts. Therefore, we also evaluate the solute and particle dynamics with a variable-ζ potential model and compare the results to a case with constant-ζ potential, assuming the particle size is large relative to the thickness of the Debye layer in each case [37].

II. MODELING EARLY-TIME DYNAMICS

Here, we describe the early-time dynamics of dissolved solute and suspended particle concentration fields in a narrow channel in the presence of a background flow that is fully developed. We develop expressions for the solute concentration c and the particle concentration n and describe approximate solutions for each.

A. Governing equations

We consider a long, narrow channel that contains solute and particles with initial concentrations $c_{\text{init}}(x)$ and $n_{\text{init}}(x)$, respectively. The initial concentrations are functions only of x; we assume, to simplify models, that the initial concentrations of both solute and particles do not vary in the spanwise direction.

The channel has a length L and height h with an aspect ratio $\epsilon = h/L \ll 1$. The channel geometry is shown in Fig. 1(a). We assume there is no slip at the walls, so the velocity profile in the channel is typical of Poiseuille flow. We further assume the flow is fully developed and therefore a function of the spanwise position y alone. To keep the dynamics of interest of the solute and particle concentrations centered in our reference frame, we shift our reference frame to move at the average velocity $\bar{U}$ such that the fluid velocity profile is given by

$$u(y) = -\frac{6\bar{U}}{h^2}\left(y^2 - \frac{h^2}{4}\right) - \bar{U}. \tag{1}$$

The concentration of a species undergoing Taylor dispersion is centered about a point that moves with the mean velocity [1], so this velocity profile keeps the dynamics centered in the moving reference frame.

The solute concentration c is governed by the advection–diffusion equation,

$$\frac{\partial c}{\partial t} = D_s \nabla^2 c - \vec{u} \cdot \nabla c, \tag{2}$$

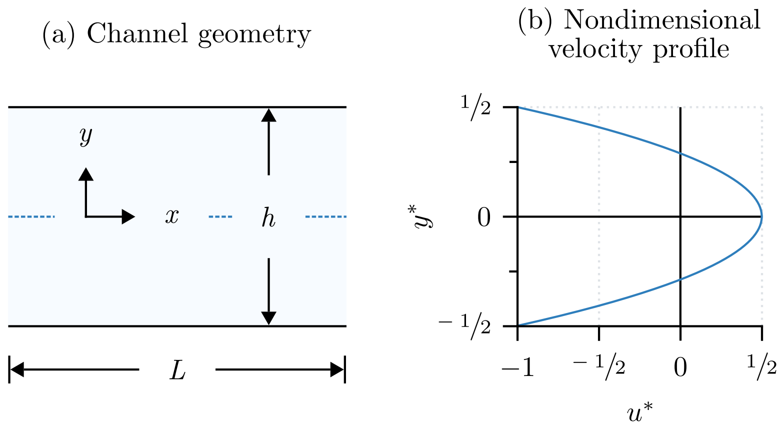

FIG. 1. The geometry of the channel and velocity profile. Image (a) shows the geometry; the aspect ratio $\epsilon = h/L$ is small and has been exaggerated in the figure. Image (b) shows the nondimensional velocity profile, which has been shifted by the average velocity to better show the relevant dynamics.

where D_s is the diffusivity of the solute. An illustration of the evolution of the solute concentration profile in a Poiseuille flow is shown in Fig. 2. Here, the solute along the channel centerline is advected downstream more rapidly than the solute near the channel walls, leading to cross-stream concentration gradients. These cross-stream gradients lead to enhanced diffusion via the typical Taylor dispersion mechanism: diffusion is enhanced by the relative motion of fluid at different radial positions y and, within the early-time regime where $t < \mathcal{O}(h^2/D_s)$, spanwise diffusion is significant.

The particle concentration n can be found in a similar manner. The particle velocity $\vec{u}_p$, however, has an additional component due to diffusiophoresis that arises from the interactions of particles with solute. The particle concentration is therefore governed by

$$\frac{\partial n}{\partial t} = D_p \nabla^2 n - \nabla \cdot (\vec{u}_p n), \tag{3}$$

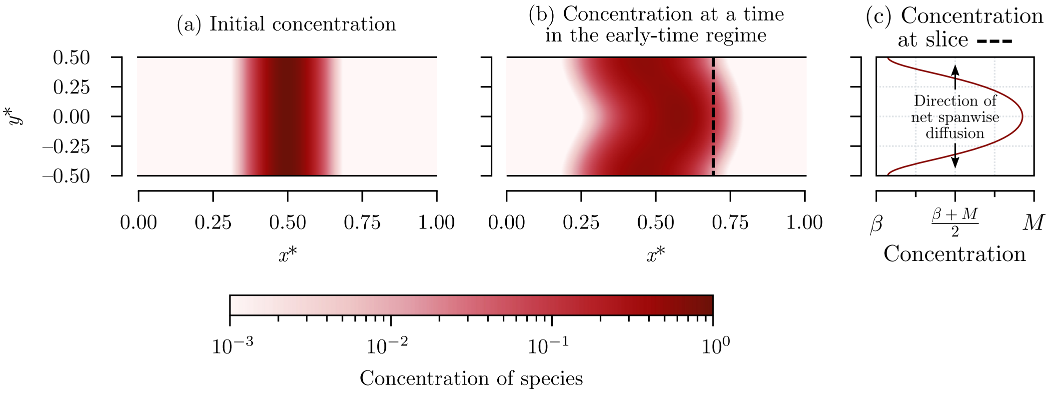

FIG. 2. An illustration of the evolution of the solute concentration in the early-time regime. The solute concentration, initially forming a Gaussian distribution in panel (a), evolves due to both advection and diffusion. After a finite time in the early-time regime, the distribution resembles that shown in panel (b). The cross-stream concentration gradients that exist because of the shear gradients in the flow lead to cross-stream diffusion and enhanced diffusion in the streamwise direction via Taylor dispersion. A slice of the concentration profile, shown in panel (c), shows the direction of net diffusion in the spanwise direction; the concentration varies between the background concentration β and a bounding value $M < 1$.

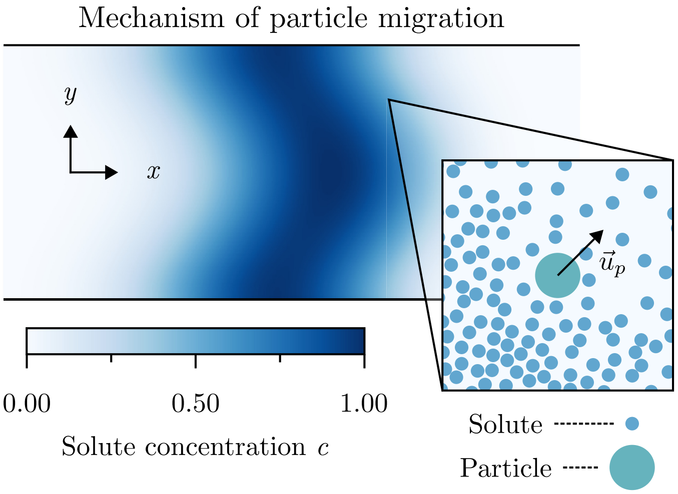

FIG. 3. The mechanism for the migration of particles. Here, the shear gradients in the Poiseuille flow introduce cross-stream gradients of the solute concentration profile. These cross-stream gradients introduce an additional cross-flow diffusiophoretic velocity to the particles. The direction of $\vec{u}_p$ has been exaggerated.

where D_p is the diffusivity of the particles, and the total velocity of the particles $\vec{u}_p$ is given by $\vec{u}_p = \vec{u} + \Gamma_p \nabla \ln c$ where Γ_p is the diffusiophoretic mobility of the particles [38]. This relationship has been confirmed in several experiments [3,10,11,39–41]. We do not consider diffusioosmotic flow at the channel walls. The mechanism for particle migration is shown in Fig. 3, which demonstrates the importance of the spanwise component of the gradient of solute concentration. Here, we assume Γ_p is constant to facilitate the theoretical modeling of the particle concentration profile. In general, the diffusiophoretic mobility is a function of particle ζ potential, which varies with conditions such as the solute concentration, temperature, and pH [34]. This assumption is discussed in Sec. V.

We nondimensionalize Eqs. (1), (2), and (3) with

$$y^* = \frac{y}{h}, \quad x^* = \frac{x}{L}, \quad u^* = \frac{u}{\bar{U}}, \quad \text{and} \quad t^* = \frac{tD_s}{h^2},$$

where we have chosen h^2/D_s as the characteristic timescale. We later discuss the extension of our theory to the long-time regime in Sec. IV. Our choice of nondimensionalization yields a nondimensional velocity profile given by

$$u^*(y^*) = -6y^{*2} + \frac{1}{2}, \tag{4}$$

which is shown in Fig. 1(b). Similarly, the governing equations for the solute and particle concentrations become, respectively,

$$\frac{\partial c}{\partial t^*} = \epsilon^2 \frac{\partial^2 c}{\partial x^{*2}} + \frac{\partial^2 c}{\partial y^{*2}} - \epsilon\, \mathrm{Pe}\, u^* \frac{\partial c}{\partial x^*} \tag{5}$$

and

$$\frac{\partial n}{\partial t^*} = \frac{D_p}{D_s}\epsilon^2 \frac{\partial^2 n}{\partial x^{*2}} + \frac{D_p}{D_s}\frac{\partial^2 n}{\partial y^{*2}} - \epsilon\, \mathrm{Pe}\, u^* \frac{\partial n}{\partial x^*} - \frac{\Gamma_p}{D_s}\epsilon^2 \frac{\partial}{\partial x^*}\left(n \frac{\partial}{\partial x^*} \ln c\right) - \frac{\Gamma_p}{D_s}\frac{\partial}{\partial y^*}\left(n \frac{\partial}{\partial y^*} \ln c\right), \tag{6}$$

where $\mathrm{Pe} = \bar{U}h/D_s$ is the Péclet number, defined as the relative balance of advection along the channel and solute diffusion across the channel. The units of concentration are arbitrary; Eqs. (5) and (6) hold regardless of the choice of units.

We seek analytical solutions by writing both concentrations as series expansions about small ϵ. The series expansions are

$$c(x^*, y^*, t^*) = c_0(x^*, y^*, t^*) + \epsilon c_1(x^*, y^*, t^*) + \epsilon^2 c_2(x^*, y^*, t^*) + \dots \tag{7}$$

and

$$n(x^*, y^*, t^*) = n_0(x^*, y^*, t^*) + \epsilon n_1(x^*, y^*, t^*) + \epsilon^2 n_2(x^*, y^*, t^*) + \dots. \tag{8}$$

We solve for the terms in each equation to acquire an approximate solution for the solute and particle concentrations. To achieve the analytical solutions given below, it will be convenient to first write the nondimensional velocity profile given in Eq. (4) as a cosine series,

$$u^*(y^*) = \sum_{\lambda=1}^{\infty} -\frac{6(-1)^\lambda}{\lambda^2 \pi^2} \cos 2\lambda\pi y^*. \tag{9}$$

This will be used for both the solute and particle concentration, for which we solve leading-order equations to acquire an approximate solution. We assume both the solute and particles have initial distributions that are dependent on x^* alone. Where numerical results are given, we assume each species has a Gaussian distribution initially, such that

$$\begin{aligned} c_{\text{init}} &= (1-\beta_c)\exp\left[-\frac{1}{2}\left(\frac{x^*-\mu_c}{\sigma_c}\right)^2\right] + \beta_c \quad \text{and} \\ n_{\text{init}} &= (1-\beta_n)\exp\left[-\frac{1}{2}\left(\frac{x^*-\mu_n}{\sigma_n}\right)^2\right] + \beta_n, \end{aligned} \tag{10}$$

with $\beta_c = 0.01$, $\mu_c = 0.5$, $\sigma_c = 0.05$, $\beta_n = 0.5$, $\mu_n = 0.5$, and $\sigma_n = 0.05$. These are centered in the channel in the x direction as a result of the choice of μ_c and μ_n. The values β_c and β_n give the background concentration of solute and particles, respectively, and are arbitrary; the governing equations hold for any units of concentration. The values σ_c and σ_n define the width of the regions of high concentration in the center of the channel. The nonzero background concentrations ensure the contribution to particle velocity from diffusiophoresis is finite.

B. Leading-order solute concentration

The leading-order solute concentration profile can be obtained by first substituting the expansion in Eq. (7) into Eq. (5). This gives

$$\begin{aligned} \frac{\partial c_0}{\partial t^*} + \epsilon \frac{\partial c_1}{\partial t^*} + \epsilon^2 \frac{\partial c_2}{\partial t^*} &= \epsilon^2 \frac{\partial^2 c_0}{\partial x^{*2}} + \epsilon^3 \frac{\partial^2 c_1}{\partial x^{*2}} + \epsilon^4 \frac{\partial^2 c_2}{\partial x^{*2}} + \frac{\partial^2 c_0}{\partial y^{*2}} + \epsilon \frac{\partial^2 c_1}{\partial y^{*2}} + \epsilon^2 \frac{\partial^2 c_2}{\partial y^{*2}} \\ &\quad - \text{Pe}\left[\epsilon u^* \frac{\partial c_0}{\partial x^*} + \epsilon^2 u^* \frac{\partial c_1}{\partial x^*} + \epsilon^3 u^* \frac{\partial c_2}{\partial x^*}\right]. \end{aligned} \tag{11}$$

At $\mathcal{O}(\epsilon^0)$, the governing equation simplifies to $\frac{\partial c_0}{\partial t^*} = \frac{\partial^2 c_0}{\partial y^{*2}}$, where the initial condition is independent of y^* as stated. Thus, the leading-order solute concentration c_0 must be independent of y^* and t^*, and the advection and streamwise diffusion terms are order ϵ or higher. With these nondimensionalizations, the leading-order solute concentration profile is simply equal to the initial condition, and all of the dynamics appear at $\mathcal{O}(\epsilon^1)$ or higher. This is primarily due to the choice of timescale in the nondimensionalization, since the evolution of the solute profile along the channel occurs over the slower timescale L^2/D_s. We will later use a multiple-timescale analysis to extend our results to the late-time regime to illustrate this development. Thus, for now, we have $c_0(x^*, y^*, t^*) = c_0(x^*) = c_{\text{init}}(x^*)$ and, by a similar argument for the particle concentration, $n_0(x^*, y^*, t^*) = n_0(x^*) = n_{\text{init}}(x^*)$. At order ϵ, Eq. (11) is

$$\text{Pe}\, u^* \frac{dc_0}{dx^*} + \frac{\partial c_1}{\partial t^*} - \frac{\partial^2 c_1}{\partial y^{*2}} = 0;$$

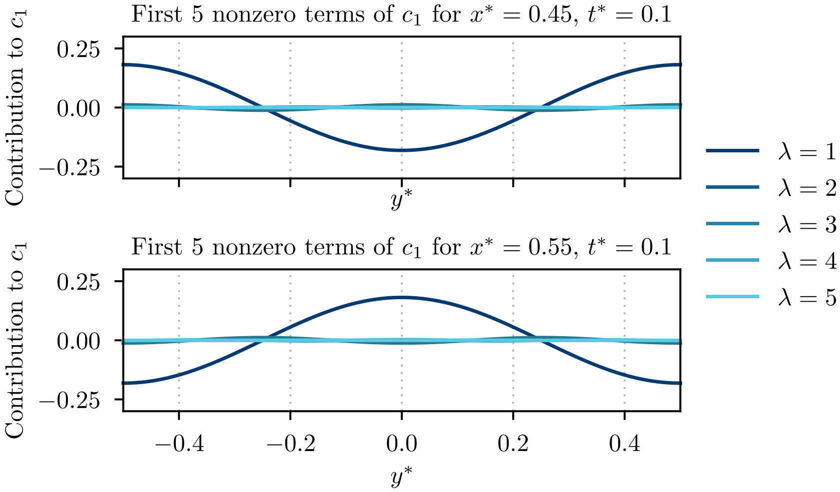

FIG. 4. The first five terms, indicated with index λ, of c_1 for $t^* = 0.1$ at two values of x^*. The initial concentrations are given in Eq. (10). The selected values x^* are $\mu_c - \sigma_c$ and $\mu_c + \sigma_c$, where $|\frac{dc_0}{dx^*}|$ is a maximum. The magnitude of contributions diminishes rapidly as λ increases. The difference in shape at the two values x^* shows the cross-flow solute concentration gradient is toward the walls to the left of the peak ($x^* = 0.45$) and toward the center of the channel to the right of the peak ($x^* = 0.55$).

the initial concentration c_0 is known, but the term c_1 must be found. We separate variables and write $c_1(x^*, y^*, t^*) = \frac{dc_0}{dx^*} F(y^*, t^*)$. This, along with the velocity profile given in Eq. (9), yields

$$\sum_{\lambda=1}^{\infty} -\frac{6\text{Pe}(-1)^{\lambda}}{\lambda^2\pi^2} \cos 2\lambda\pi y^* + \frac{\partial F}{\partial t^*} - \frac{\partial^2 F}{\partial y^{*2}} = 0,$$

which has no dependence on x^*. We now seek a solution of the form

$$F(y^*, t^*) = \sum_{\lambda=0}^{\infty} a_{\lambda}(t^*) \cos 2\lambda\pi y^*.$$

This yields

$$a_0'(t^*) = 0 \quad \text{and} \quad -\frac{6(-1)^{\lambda}}{\lambda^2\pi^2} + a_{\lambda}'(t^*) + 4\lambda^2\pi^2 a_{\lambda}(t^*) = 0, \quad \lambda = 1, 2, 3, \ldots;$$

since $F(t^* = 0) = 0$ to maintain an initial concentration that is dependent only on x^*, we require that $a_{\lambda}(0) = 0$. The solutions are then

$$a_0(t^*) = 0 \quad \text{and} \quad a_{\lambda}(t^*) = \frac{3\,\text{Pe}\,(-1)^{\lambda}}{2\lambda^4\pi^4}[1 - \exp(-4\lambda^2\pi^2 t^*)], \quad \lambda = 1, 2, 3, \ldots.$$

With these coefficients, the solution for the solute concentration is defined to $\mathcal{O}(\epsilon^1)$. The first five terms λ of $(c_1)_{\lambda} = \frac{dc_0}{dx^*} F_{\lambda}$ are shown at $t^* = 0.1$ for selected slices of x^* to the right and left of the peak concentration in Fig. 4. The magnitude of the terms decreases rapidly with increasing λ, and nearly all of the variation is captured by the first term. Furthermore, we see that the cross-stream solute concentration gradient reverses sign to the left and right of the peak, suggesting that the cross-stream diffusiophoretic velocity also changes direction from the upstream to downstream relative to the solute peak. That is, depending on the sign of Γ_p, particles are expected to focus either at the channel center or at the walls upstream of the peak and viceversa downstream of the peak.

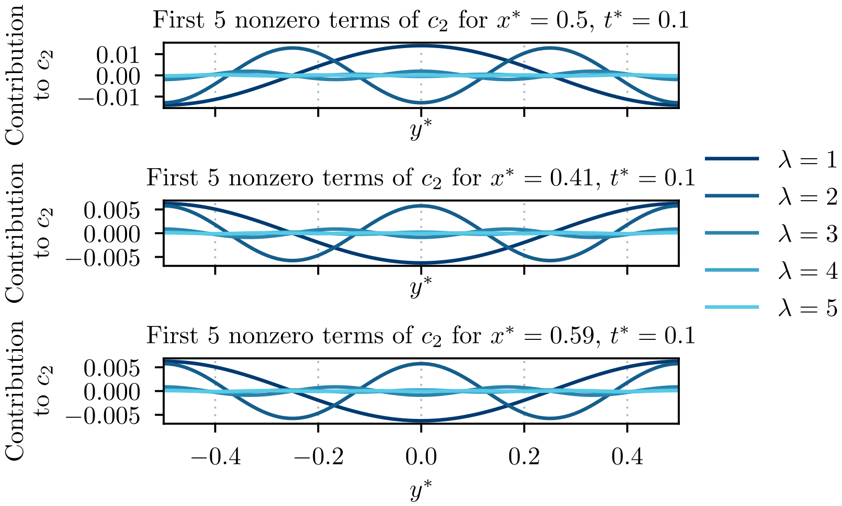

FIG. 5. The first five terms of c_2 for $t^* = 0.1$ at values of x^* where $|\frac{d^2c_0}{dx^{*2}}|$ is a maximum. The initial concentrations are given in Eq. (10). The magnitude of each term is small relative to the first term in c_1.

C. Higher-order solute concentration

We now extend our approach to seek the next higher-order correction to the solute concentration profile. The next leading-order equation is

$$\frac{\partial c_2}{\partial t^*} = \frac{\partial^2 c_2}{\partial y^{*2}} + \frac{d^2 c_0}{dx^{*2}} - \mathrm{Pe}\, u^* \frac{\partial c_1}{\partial x^*}.$$

As before, we separate variables and consider $c_2 = \frac{d^2c_0}{dx^{*2}} G(y^*, t^*)$, which eliminates dependence on nondimensional streamwise position x^* and yields

$$\frac{\partial G}{\partial t^*} = \frac{\partial^2 G}{\partial y^{*2}} + 1 - \mathrm{Pe}\, u^* F(y^*, t^*). \tag{12}$$

The details of the calculation of G are given in Appendix A. The solute concentration is now defined to $\mathcal{O}(\epsilon^2)$ with the initial concentration c_0 and the series c_1 and c_2. The first five terms λ of $(c_2)_\lambda = \frac{d^2c_0}{dx^{*2}} G_\lambda$ are shown at various x^* in Fig. 5. The magnitudes of terms in c_2 appear small relative to terms in c_1, and the higher order of ϵ associated with c_2 further lessens its contribution to c. For the purposes of predicting the particle dynamics, we see that this theoretical prediction for the solute concentration profile is of sufficiently high order, since it captures the cross-stream solute concentration gradients that drive the two-dimensional particle effects. These distinguish this work from the long-time behaviors previously studied, in which the cross-stream behaviors are effectively averaged out and the results become quasi-one-dimensional. In Sec. II D, we extend our analysis to predict the particle concentration dynamics that are dependent on this solute concentration profile.

D. Particle concentration

We follow a solution approach similar to that used for the solute concentration to solve for the particle concentration profile. Here, the leading-order equation of interest is

$$\frac{\partial n_1}{\partial t^*} = -\frac{\Gamma_p}{D_s} \frac{n_0(x^*)}{c_0(x^*)} \frac{\partial^2 c_1}{\partial y^{*2}} - \mathrm{Pe}\, u^* \frac{\partial n_0}{\partial x^*}.$$

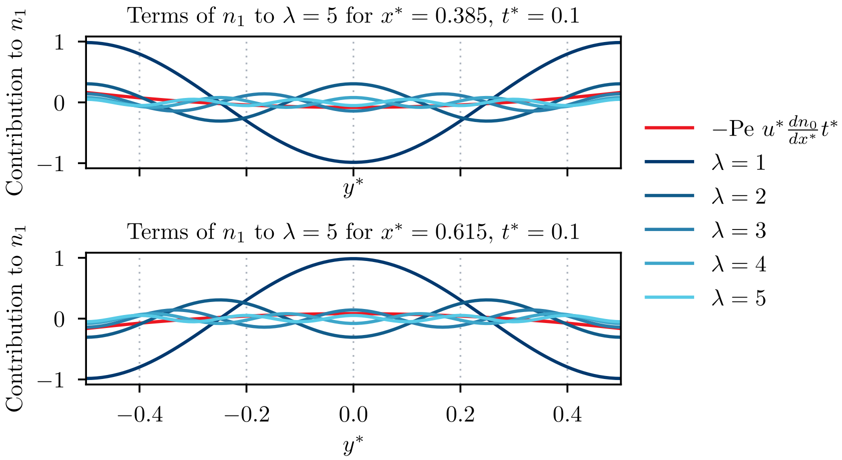

FIG. 6. The terms of n_1 to $\lambda = 5$ for $t^* = 0.1$ at values of x^* where $|\frac{n_0}{c_0}\frac{dc_0}{dx^*}|$ is a maximum. The initial concentrations are given in Eq. (10). The largest contribution is from the $\lambda = 1$ term.

Following the approach above, the solution to this is

$$n_1(x^*, y^*, t^*) = -\frac{\Gamma_p}{D_s}\frac{n_0}{c_0}\frac{dc_0}{dx^*}\sum_{\lambda=1}^{\infty}\frac{-6\mathrm{Pe}(-1)^\lambda}{\lambda^2\pi^2}\left[\frac{\exp(-4\lambda^2\pi^2t^*)}{4\lambda^2\pi^2} + t^*\right]\cos(2\lambda\pi y^*)$$
$$- \mathrm{Pe}\, u^*\frac{dn_0}{dx^*}t^* + N_1(x^*, y^*).$$

With $n_1(x^*, y^*, 0) = 0$, we have

$$N_1(x^*, y^*) = -\frac{\Gamma_p}{D_s}\frac{n_0}{c_0}\frac{dc_0}{dx^*}\sum_{\lambda=1}^{\infty}\frac{3\mathrm{Pe}(-1)^\lambda}{2\lambda^4\pi^4}\cos 2\lambda\pi y^*.$$

Extending the solution to the next-highest order is nontrivial. However, here the solution already captures the two-dimensional effects to leading order, and additional terms are expected to be small relative to the $\mathcal{O}(\epsilon)$ term, as observed with c_1 and c_2 in Sec. II C. The largest contribution to n_1 is from the first few terms, as shown in Fig. 6. The contribution from terms decreases with increasing λ.

III. NUMERICAL SOLUTIONS FOR CONCENTRATIONS

We use numerical simulations to calculate the concentration profiles of both the solute and particles. The solute and particle concentrations are found by numerically solving Eqs. (5) and (6), respectively. The results give insight into the dynamics of each species and provide a basis for comparison with the analytical solutions.

A. Overview and approach

We calculate the concentrations of the solute and particles numerically using a simple finite difference approach with first-order accuracy in time and second-order accuracy in space. Numerical results in Sec. VI use a 601 × 61 discretized grid. The time step for all simulations is $\Delta t^* = (\Delta y^*)^2/20$, where the factor of $1/20$ is included to guarantee stability. This is smaller than the typical factor of $1/2$ required by the Courant–Friedrichs–Lewy condition due to the extra nonlinear diffusiophoresis term; this factor of safety was found to work well in ensuring convergence.

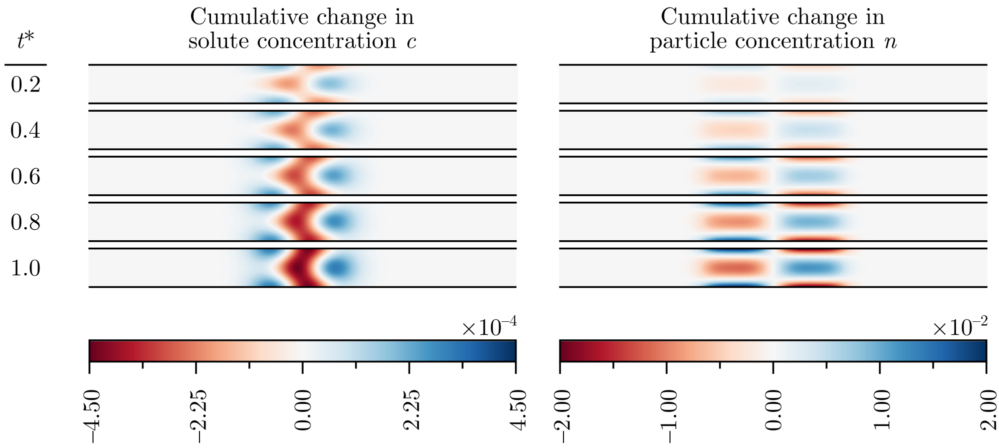

FIG. 7. The cumulative change in concentrations (the difference between the current and initial concentrations) after a time t^* with $\mathrm{Pe} = 1$, $\epsilon = 10^{-3}$, $\Gamma_p/D_s = 1$, and $D_p/D_s = 10^{-3}$, based on numerical simulations. The solute and particle concentrations have Gaussian distributions initially; the initial concentrations are given in Eq. (10). The evolution of the solute concentration is characteristic of a species experiencing advection and diffusion. The particle concentration, however, shows a significantly different focusing behavior due to the diffusiophoresis. In addition to having a significantly faster growing solution, the particle concentration also expands more quickly along x^* and shows a reversed focusing behavior in front of and behind the peak.

We use second-order no-flux boundary conditions along the top and bottom of the channel for both solute and particle fields; that is, we enforce $\frac{\partial c}{\partial y^*}|_{y^*=\pm 1/2} = 0$ and $\frac{\partial n}{\partial y^*}|_{y^*=\pm 1/2} = 0$. We impose zero-gradient solute and particle concentration fields at the inlet and outlet with $\frac{\partial c}{\partial x^*}|_{x^*\in\{0,1\}} = 0$ and $\frac{\partial n}{\partial x^*}|_{x^*\in\{0,1\}} = 0$. Here, the concentration does not change appreciably over the times we consider and for the initial concentrations used in Sec. VI, and local concentration gradients therefore remain small at the inlet and outlet. That is, the concentrations of solute and particles do not change appreciably at the entrance and exit of the channel over the values of t^* used in simulations. We ascertain that the numerical solutions have converged with a convergence study given in Appendix E.

B. Results

The results of numerical simulations for several values of t^* are given in Fig. 7 for $\mathrm{Pe} = 1$, $\epsilon = 10^{-3}$, $\Gamma_p/D_s = 1$, and $D_p/D_s = 10^{-3}$. The evolution of the solute concentration profile is intuitive for the background Poiseuille flow; the increase in concentration in the streamwise direction at the center of the channel is expected for a parabolic velocity profile. The changes in the particle concentration profile are notably different in shape and sign—though this may vary with different choices for parameters such as the diffusiophoretic mobility [2]—as a result of diffusiophoresis. In the absence of diffusiophoresis, the change in particle concentration would resemble that of the solute. The difference between the solute and particle dynamics suggests that two-dimensional structures in the particle distribution develop in the early-time regime where t is on the order of h^2/D_s. These structures may persist for a significant time because of the significant difference between solute and particle diffusivity.

IV. EXTENDING THE ANALYSIS TO LONG TIMES

The analysis in Sec. II is valid only within the early-time regime of order h^2/D_s. The model does not extend to long times; a multiple-timescale approach is necessary to recover the long-time solute and particle behaviors. Whereas the previous approach was fully general to any initial condition (with the limitation that it is uniform in y^*), here we limit ourselves to a single precise initial condition to illustrate the multiple-timescale approach that can be expanded for more general initial conditions. Here, except for the leading-order solute and particle concentration solutions, we have maintained generality to help the reader extend this approach to other initial conditions. To illustrate the process, we choose initial conditions of $c_{\text{init}}(x^*) = n_{\text{init}}(x^*) = \exp(-x^{*2})$ and note that the nondimensional governing equation for the solute concentration can be written as, from Eq. (5),

$$\frac{\partial c}{\partial t^*} = \epsilon^2 \frac{\partial^2 c}{\partial x^{*2}} + \frac{\partial^2 c}{\partial y^{*2}} - \epsilon^2 \,\text{Pe}_L\, u^* \frac{\partial c}{\partial x^*}, \tag{13}$$

where here we have selected the different Péclet number $\text{Pe}_L = \bar{U}L/D_s$ defined with the channel length L for convenience. The early timescale h^2/D_s and the timescale for diffusion along the channel, L^2/D_s, are separated by a factor of $\epsilon^2 = h^2/L^2 \ll 1$. We therefore introduce a second time variable, $T^* = \epsilon^2 t^*$, to describe the long-time dynamics. We can then map any time-dependent quantity as

$$f(t^*) \mapsto f(t^*, T^*) \quad \text{with} \quad \frac{\partial f}{\partial t^*} \mapsto \frac{\partial f}{\partial t^*} + \epsilon^2 \frac{\partial f}{\partial T^*}. \tag{14}$$

With this mapping, Eq. (13) becomes

$$\frac{\partial c}{\partial t^*} + \epsilon^2 \frac{\partial c}{\partial T^*} + \epsilon^2 \,\text{Pe}_L\, u^* \frac{\partial c}{\partial x^*} = \epsilon^2 \frac{\partial^2 c}{\partial x^{*2}} + \frac{\partial^2 c}{\partial y^{*2}}, \tag{15}$$

and we can write the solute concentration as the series $c(x^*, y^*, t^*, T^*) = c_0(x^*, y^*, t^*, T^*) + \epsilon^2 c_1(x^*, y^*, t^*, T^*) + \epsilon^4 c_2(x^*, y^*, t^*, T^*) + \mathcal{O}(\epsilon^6)$. Note that this expansion does not include odd powers of ϵ, which were present in Sec. II, because no such terms appear in Eq. (13) with the choice of Péclet number Pe_L. The details of the calculation of c_0 and c_1 are given in Appendix B1. The leading-order terms for the solute concentration are

$$\begin{aligned} c_0(x^*, t^*) &= \frac{1}{\sqrt{1 + 4\epsilon^2 t^*}} \exp\left(-\frac{x^{*2}}{1 + 4\epsilon^2 t^*}\right) \quad \text{and} \\ c_1(x^*, y^*, t^*) &= \text{Pe}_L \frac{\partial c_0}{\partial x^*}\left[-\frac{1}{480}(7 - 120 y^{*2} + 240 y^{*4}) \right. \\ &\quad \left. - \sum_{\lambda=1}^{\infty} \frac{3(-1)^\lambda}{2\lambda^4\pi^4} \exp[-(2\lambda\pi)^2 t^*] \cos(2\lambda\pi y^*)\right]. \end{aligned}$$

As a final step in solving for the leading-order solute concentration profiles c_0 and c_1, we undo the mapping and replace each T^* with $\epsilon^2 t^*$. Here, we can see that the leading-order solute concentration c_0 only evolves with $\epsilon^2 t^*$. That is, the time for the evolution of c_0 is $t^* \sim \mathcal{O}(\epsilon^{-2}) \gg 1$, illustrating the slow dynamics of spreading along the channel.

The same approach can be used to describe the long-time behavior of the particles by considering Eq. (6) with the new Péclet number Pe_L. With the transformation in Eq. (14), this is

$$\begin{aligned} \frac{\partial n}{\partial t^*} + \epsilon^2 \frac{\partial n}{\partial T^*} = \frac{D_p}{D_s}\left(\epsilon^2 \frac{\partial^2 n}{\partial x^{*2}} + \frac{\partial^2 n}{\partial y^{*2}}\right) - \text{Pe}_L\, \epsilon^2 u^* \frac{\partial n}{\partial x^*} - \frac{\Gamma_p}{D_s}\epsilon^2 \frac{\partial}{\partial x^*}\left(\frac{\partial \ln c}{\partial x^*} n\right) \\ - \frac{\Gamma_p}{D_s}\frac{\partial}{\partial y^*}\left(\frac{\partial \ln c}{\partial y^*} n\right). \end{aligned}$$

We expand the particle concentration as $n(x^*, y^*, t^*, T^*) = n_0(x^*, y^*, t^*, T^*) + \epsilon^2 n_1(x^*, y^*, t^*, T^*) + \epsilon^4 n_2(x^*, y^*, t^*, T^*) + \mathcal{O}(\epsilon^6)$. The details of the calculation of n_0 and n_1

are given in Appendix B 2. The resulting solution for the particle concentration is

$$n(x^*, y^*, t^*) = n_0(x^*, t^*) + \epsilon^2\big[n_1^\infty(x^*, y^*, t^*) + \hat{n}_1(x^*, y^*, t^*) + \tilde{n}_1(x^*, y^*, t^*)\big].$$

The term n_0 is

$$n_0(x^*, t^*) = \frac{\exp\left[-[B(t^*)]^{-1}\left(1+\frac{\Gamma_p}{D_s}\right)(1+4\epsilon^2 t^*)^{\frac{\Gamma_p}{D_s}} x^{*2}\right]}{\sqrt{B(t^*)(1+4\epsilon^2 t^*)^{-\frac{\Gamma_p}{D_s}}\left(1+\frac{\Gamma_p}{D_s}\right)^{-1}}},$$

with

$$B(t^*) = 1 + \frac{\Gamma_p}{D_s} + \frac{D_p}{D_s}\left[-1 + (1+4\epsilon^2 t^*)^{1+\frac{\Gamma_p}{D_s}}\right],$$

while n_1 has components

$$n_1^\infty(x^*, y^*, t^*) = -\frac{\mathrm{Pe}_L}{480}\frac{D_s}{D_p}\frac{1}{c_0}(7 - 120y^{*2} + 240y^{*4})\left(\frac{\Gamma_p}{D_s}n_0\frac{\partial c_0}{\partial x^*} + c_0\frac{\partial n_0}{\partial x^*}\right),$$

$$\hat{n}_1(x^*, y^*, t^*) = \sum_{\lambda=1}^{\infty} a_\lambda(x^*, t^*)\exp[-(2\lambda\pi)^2 t^*]\cos(2\lambda\pi y^*), \quad \text{and}$$

$$\tilde{n}_1(x^*, y^*, t^*) = \sum_{\lambda=1}^{\infty}\frac{3(-1)^\lambda D_s\,\mathrm{Pe}_L}{2D_p(D_p - D_s)\lambda^4\pi^4}\left[\Gamma_p\frac{n_0}{c_0}\frac{\partial c_0}{\partial x^*} + (D_s - D_p)\frac{\partial n_0}{\partial x^*}\right]$$
$$\times \exp\left[\frac{-(2\lambda\pi)^2 t^* D_p}{D_s}\right]\cos(2\lambda\pi y^*),$$

where

$$a_\lambda(x^*, t^*) = -\frac{3(-1)^\lambda}{2\lambda^4\pi^4}\mathrm{Pe}_L\frac{n_0}{c_0}\frac{\partial c_0}{\partial x^*}\frac{\Gamma_p/D_s}{D_p/D_s - 1}.$$

As with the solution for the solute concentration, after we solve for the leading-order terms n_0, n_1^∞, $\hat{n}_1$, and $\tilde{n}_1$, we finally undo the mapping by replacing each T^* with $\epsilon^2 t^*$ to recover the final solution. As mentioned, here we have used a simple Gaussian initial condition to illustrate the multiple-timescale approach, whereas the early-time solution approach described above remains general with respect to the initial condition. The early-time results, shown in Fig. 8, demonstrate the same behavior described in earlier sections: two-dimensional structures in the particle concentration profile develop quickly over the early timescale h^2/D_s. Here, where t^* is $\mathcal{O}(1)$, the early-time dynamics occur, and the particle dynamics evolve to approach the long-time behavior captured by n_1^∞ alone, which decays where t^* is $\mathcal{O}(\epsilon^{-2})$. This long-time behavior is illustrated in Fig. 9, where the results first show a focusing of the particles in the axial direction, corresponding to the diffusiophoretic timescale in the flow direction. After this, the cross-stream variation (and indeed the full particle concentration itself) decays over the timescale $t^* > \mathcal{O}(\epsilon^{-2})$. The variations in particle concentration decay as expected because of the inclusion of terms associated with the long timescale in this analysis.

V. COMMENTING ON THE ASSUMPTION OF CONSTANT-ζ POTENTIAL

The analytical solutions previously developed for the particle concentration are based on an assumption of constant particle ζ potential. However, in many practical systems of interest, the ζ potential is variable; it is a function of parameters such as the background solute concentration and pH. Kirby and Hasselbrink [34] discuss the variable-ζ potential of silica. They describe two scalings for the ζ potential, based on the counterion concentration in the supporting univalent electrolytes,

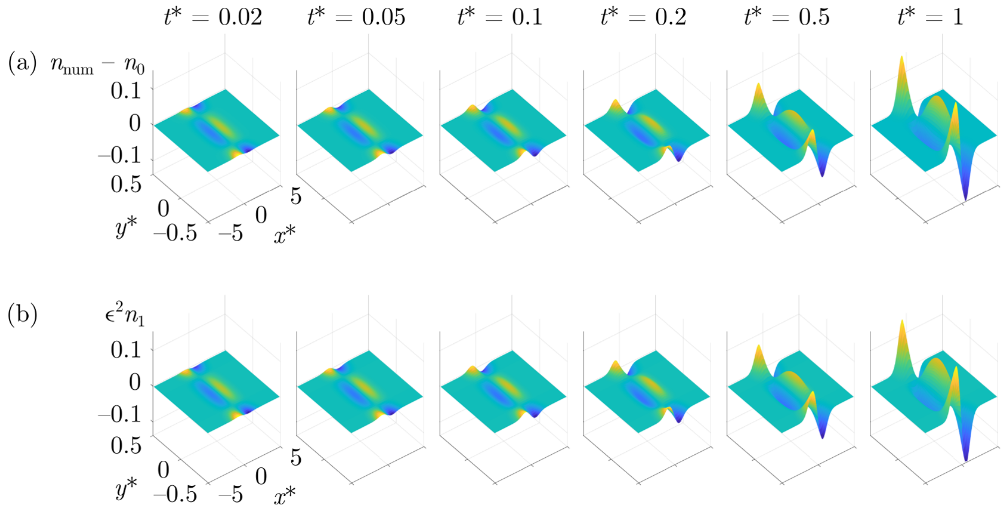

FIG. 8. Comparison between (a) the numerical result for the leading-order particle concentration variation in the channel $n_{\text{num}} - n_0$ and (b) the theoretical prediction given by $\epsilon^2 n_1$. The particle variation across the channel quickly develops over the timescale h^2/D_s. Here, $D_p/D_s = 10^{-3}$, $\Gamma_p/D_s = 1$, $\epsilon = 0.1$, and $\text{Pe}_L = 10$. Details of calculations are provided in Appendix B 3.

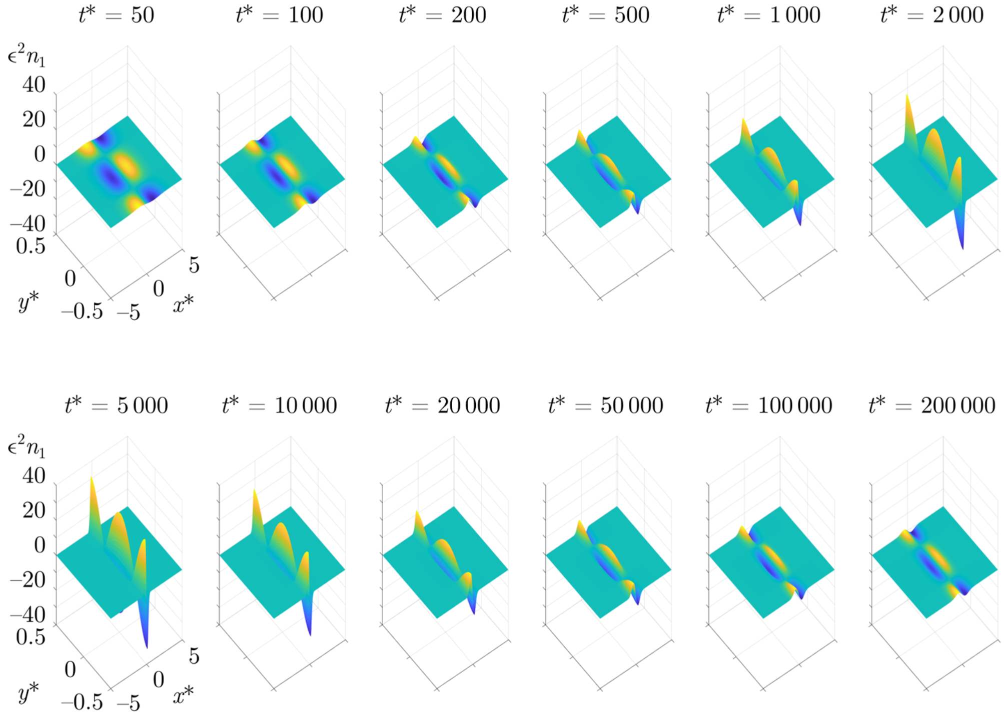

FIG. 9. Visualization of the long-time behavior of the particle concentration up to $t^* = 5000$ (corresponding to 50 of the slow-time units $\epsilon^2 t^*$). There is first a focusing in the axial direction. This corresponds to the diffusiophoretic timescale along the flow, after which there is a smoothing decay of the cross-stream variation over the slow timescale. Here, $D_p/D_s = 10^{-3}$, $\Gamma_p/D_s = 1$, $\epsilon = 0.1$, and $\text{Pe}_L = 10$. Details of calculations are provided in Appendix B 3.

for both high and low ζ. The high-ζ limit, which the researchers claim to be better for general applications, has the form

$$\zeta = m_0 + m_1 \log_{10} \sum_k c_k,$$

where c_k is the concentration of a counterionic species in mM and the values m_0 and m_1 are found experimentally [34]. We consider the ionic species Na^+ and Cl^-, corresponding to diffusion coefficients $D_+ = 1.33 \times 10^{-9}\,\mathrm{m}^2\,\mathrm{s}^{-1}$ and $D_- = 2.03 \times 10^{-9}\,\mathrm{m}^2\,\mathrm{s}^{-1}$, respectively [3]. Shin *et al.* [3] give expressions for β, D_s, and Γ_p, from which we find $\beta = (D_+ - D_-)(D_+ + D_-)^{-1} = -2.08 \times 10^{-1}$, $D_s \equiv (2D_+D_-)(D_+ + D_-)^{-1} = 1.61 \times 10^{-9}\,\mathrm{m}^2\,\mathrm{s}^{-1}$, and

$$\Gamma_p = \frac{\varepsilon}{\mu}\left(\frac{k_BT}{Ze}\right)^2\left(\beta\frac{Ze\zeta}{k_BT} + 4\ln\cosh\frac{Ze\zeta}{4k_BT}\right), \tag{16}$$

where $\varepsilon = \varepsilon_0\varepsilon_r$ is the permittivity of the medium, μ its viscosity, T its absolute temperature, and k_B the Boltzmann constant. Here, for illustration, we assume the Debye layers are thin relative to the size of the particles, which reduces the complexity of potential calculations by neglecting size effects [37]. In general, the Debye layer thickness is also a function of the background solute concentration which can be accounted for, but for the purposes of highlighting the differences between the variable- and constant-ζ potential models, this is unnecessary in the current work. The permittivity is estimated with a relative permittivity of $\varepsilon_r = 78.4$, based on water at $T = 25^\circ = 298.15\,\mathrm{K}$ [42]. We estimate the viscosity as $\mu = 8.9 \times 10^{-4}\,\mathrm{Pa}\cdot\mathrm{s}$ and use a vacuum permittivity of $\varepsilon_0 = 8.854 \times 10^{-12}\,\mathrm{F\,m}^{-1}$, Boltzmann constant $k_B = 1.381 \times 10^{-23}\,\mathrm{J\,K}^{-1}$, and charge $Ze = e = 1.602 \times 10^{-19}\,\mathrm{C}$.

From Kirby and Hasselbrink [34, Fig. 3], we note that $m_0 = 0$ and estimate a value $m_1 = 53.7\,\mathrm{mV}$ (based on an aqueous solution with counterion Na^+ at $T = 25^\circ = 298.15\,\mathrm{K}$). For comparison between cases of constant and variable particle ζ potential, we use an initial solute concentration c_0 that varies between 0.1 mM and 10 mM; this is within the range of concentration considered by Kirby and Hasselbrink [34] that we use to estimate m_1. We therefore define the initial solute and particle concentrations as

$$c_0(x^*) = M_c\left\{(1-\beta_c)\exp\left[-\frac{1}{2}\left(\frac{x^*-\mu_c}{\sigma_c}\right)^2\right] + \beta_c\right\} \quad \text{and}$$

$$n_0(x^*) = (1-\beta_n)\exp\left[-\frac{1}{2}\left(\frac{x^*-\mu_n}{\sigma_n}\right)^2\right] + \beta_n, \tag{17}$$

with $M_c = 0.01$, $\beta_c = 0.01$, $\mu_c = 0.5$, $\sigma_c = 0.05$, $\beta_n = 0.5$, $\mu_n = 0.5$, and $\sigma_n = 0.05$. These are the similar to the initial concentrations used previously, except we have scaled c_0 to work with the empirical relationship of [34], since it requires solute concentration in mM. For this comparison, we assume the particles are spherical with radius $1\,\mu\mathrm{m}$ and the Reynolds number is small. The particle diffusivity is estimated with the Stokes–Einstein equation [43] as $D_p = k_BT/(6\pi\mu r) \approx 2.45 \times 10^{-13}\,\mathrm{m}^2\,\mathrm{s}^{-1}$.

For the case with constant particle ζ potential, we calculate ζ by finding the mean value based on the initial concentration profile. We first calculate ζ from the initial solute concentration and take the mean. This yields a mean-ζ potential in our system of $\zeta \approx -0.138\,\mathrm{V}$, from which we find an effective diffusiophoretic mobility of $\Gamma_p \approx 2.10 \times 10^{-9}\,\mathrm{m}^2\,\mathrm{s}^{-1}$. We then reproduce the calculation using a variable-ζ potential model using the previously described model of Kirby and Hasselbrink [34]. The results of a comparison of constant- and variable-ζ potential models are provided in Fig. 10. The particle concentration profiles that result from the two different models show reasonable qualitative and quantitative agreement with some distinct features. In particular, one key difference between the two predictions is the relative lack of particle focusing near the center of the channel $x^* \sim 0.5$. Thus, in this particular example, we see that the greatest difference

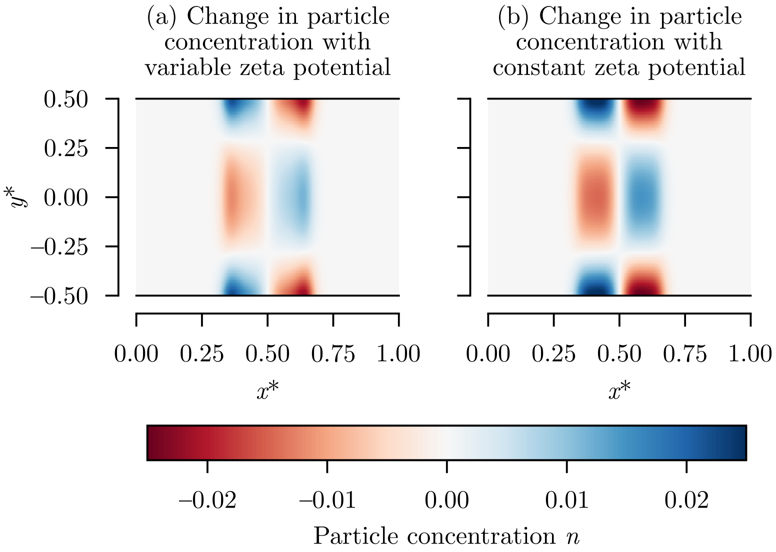

FIG. 10. The change in particle concentration n at $t^* = 1$ with $\mathrm{Pe} = 1$ and $\epsilon = 10^{-3}$. The initial concentrations are given in Eq. (17). Particle concentrations are calculated with numerical simulations. Image (a) shows the concentration when the particle ζ potential varies as $\zeta = m_1 \log_{10} c$; image (b) shows the concentration with constant-ζ potential, calculated as the mean-ζ potential associated with the initial solute concentration c_0.

in the predictions of the two models occurs where the background solute concentration is expected to be greatest—that is, near the center of the initial Gaussian peak. A physical explanation for this can be seen by calculating the spatial variation in ζ and Γ_p for the variable-ζ potential model. This spatial variation in ζ and Γ_p can be seen in Fig. 11, where we see that the relative minimum in both ζ and Γ_p occurs precisely in the region of largest solute concentration. This region of relatively low diffusiophoretic mobility can account for the relative lack of particle focusing either at the channel walls or channel center in the region near the peak that was seen in Fig. 10. Since the cross-channel solute concentration gradients are independent of the choice of ζ potential model, the diffusiophoretic velocity of particles near $x^* \sim 0.5$, where Γ_p is small, is expected to be small in the variable-ζ potential model.

Thus, in comparing the predictions of both the constant- and variable-ζ potential models, we recognize that, based on the model of Kirby and Hasselbrink [34], the assumption of constant-ζ potential strictly applies only where absolute solute concentrations or concentration gradients are small. However, even in this specific system, where the solute concentration varies by two orders of magnitude and both ζ and Γ_p vary by over 100% throughout the system, the qualitative and quantitative particle focusing behaviors for the two models shown in Fig. 10 have reasonable agreement. One exception to this is at the solute concentration peak, where the diffusiophoretic mobility has the greatest deviation from the value associated with the mean-ζ potential. The diffusiophoretic focusing is a highly nonlinear process, especially when the variable-ζ potential is considered, and we must remember that it is always also coupled to the particle diffusion, which will ultimately limit the degree of focusing. These facts complicate the determination of specific statements on the applicability of the constant-ζ potential assumption. However, if we consider the early-time dynamics of specific systems where particle diffusiophoresis dominates over particle diffusion, then clearly the rate of particle focusing is proportional to the diffusiophoretic velocity, which is proportional to Γ_p. Thus, if the spatially varying local Γ_p differs from the calculated Γ_p based on the mean ζ by a given percentage, then the rate of particle focusing predicted by the constant-ζ potential model should be expected to have errors on the same order of magnitude as that deviation. Beyond this general guideline, more specific statements about the validity of the

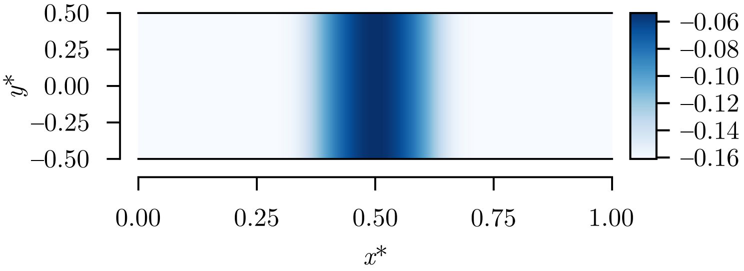

(a) ζ from initial concentration (V)

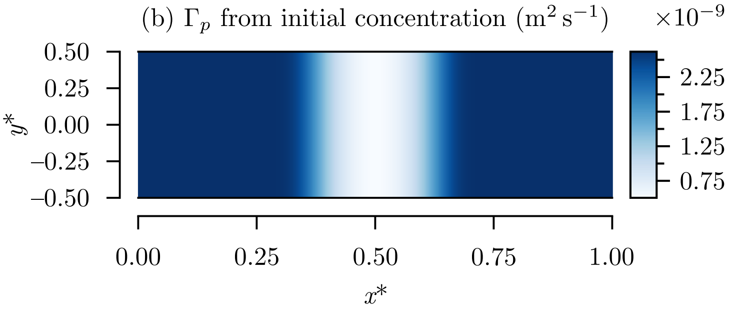

(b) Γ_p from initial concentration ($\mathrm{m^2\,s^{-1}}$)

FIG. 11. The particle ζ potential, shown in panel (a), and diffusiophoretic mobility Γ_p, shown in panel (b). The initial concentrations are given in Eq. (17). The mean value of ζ is used for the case of constant-ζ potential. Both ζ and Γ_p have significant variation over the channel length.

constant-ζ potential model can be informed by performing a similar simulations over a range of various initial conditions, geometries, and flow parameters, which is an interesting study that we will continue to investigate in future work.

VI. DISCUSSION

To validate our theoretical predictions for the early-time dynamics, we compare the predictions with numerical simulations. We choose $\mathrm{Pe} = 1$, $\epsilon = 10^{-3}$, $\Gamma_p/D_s = 1$, and $D_p/D_s = 10^{-3}$ for an example calculation. These parameters correspond to particles with very low diffusivity relative to the solute, which is expected for particles of size 1 μm and larger, and with a diffusiophoretic mobility on the same order as the diffusivity of the solute. A comparison of results from numerical solutions and analytical approximations is given in Fig. 12, which shows how solute and particle concentrations evolve upstream and downstream of the solute peak and demonstrates agreement between the theoretical predictions and the numerical simulations. An additional comparison with $\mathrm{Pe} = 50$ is presented in Fig. 13. At early times t^* and relatively low values of ϵ and Pe, the analytical results match the numerical solutions closely, which suggests that the models accurately capture the solute and particle dynamics over this range of parameters. Note that, strictly speaking, the early-time model also requires that $\epsilon\,\mathrm{Pe}$ be small, which is why we have used a smaller value of ϵ in Fig. 13.

To quantitatively evaluate the performance of the models, we compare the analytical and numerical results for several values of ϵ and Pe, keeping all else constant and utilizing the same initial concentration distributions. We calculate relative error assuming the numerical results are correct. This does not provide a comprehensive view of the accuracy of the analytical results; the concentrations are, of course, also dependent on the initial distribution of solute and particles, and on parameters like diffusivity and diffusiophoretic mobility, which vary by species. It does, however, show how changing the aspect ratio or Péclet number affects the results. Estimates of the

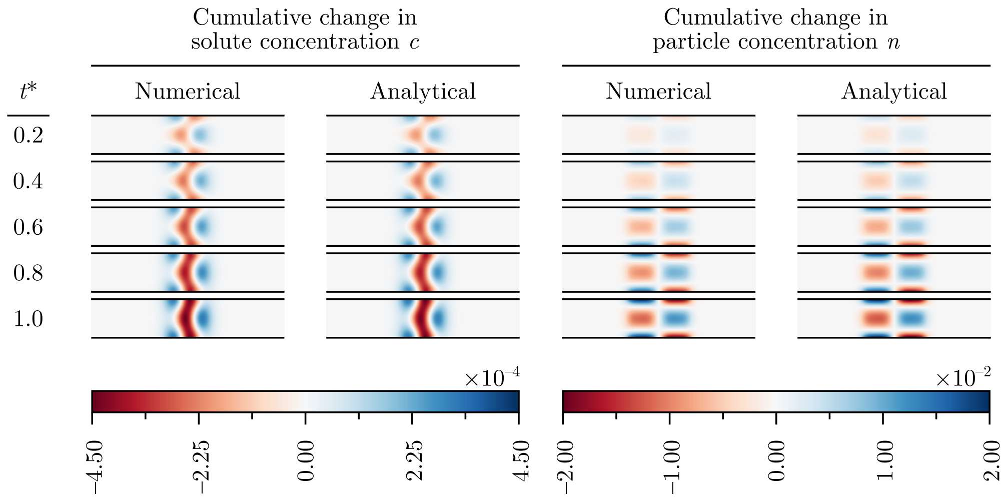

FIG. 12. The cumulative change in concentration (the difference between the current and initial concentrations) after a time t^* with Pe $= 1$, $\epsilon = 10^{-3}$, $\Gamma_p/D_s = 1$, and $D_p/D_s = 10^{-3}$. The initial concentrations are given in Eq. (10). The numerical and analytical results match closely.

error are provided in Fig. 14. Intuitively, the error tends to increase with increasing ϵ—likely a result of increasing truncation error in the perturbation series and a breakdown in the lubrication approximation—and with increasing Pe.

The analytical solutions that we have presented here are for the coupled solute–particle–fluid dynamics in a simple two-dimensional geometry with a pressure-driven flow. The dynamics in more complex geometries, including cross-sections of three-dimensional channels or channels with pores or junctions, such as those considered by Shin *et al.* [10,3] and Ault *et al.* [23], or in situations with other effects like moving boundaries and diffusioosmotic flow, are more complex and would necessitate modifications to our models. However, the methods and theoretical approach we have presented here can be extended and applied to more complicated systems and are relevant to flows

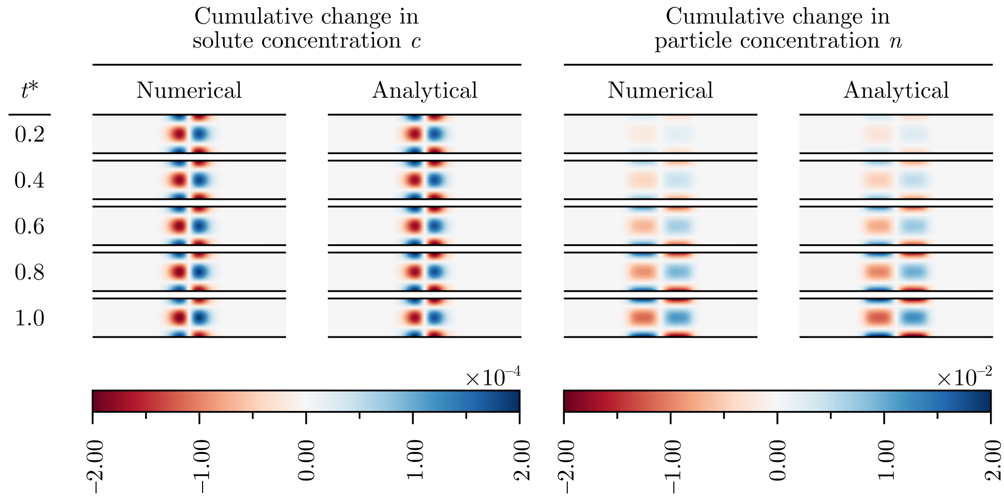

FIG. 13. The cumulative change in concentration as a function of t^* with Pe $= 50$, $\epsilon = 2 \times 10^{-5}$, $\Gamma_p/D_s = 1$, and $D_p/D_s = 10^{-3}$. The numerical and analytical results match closely.

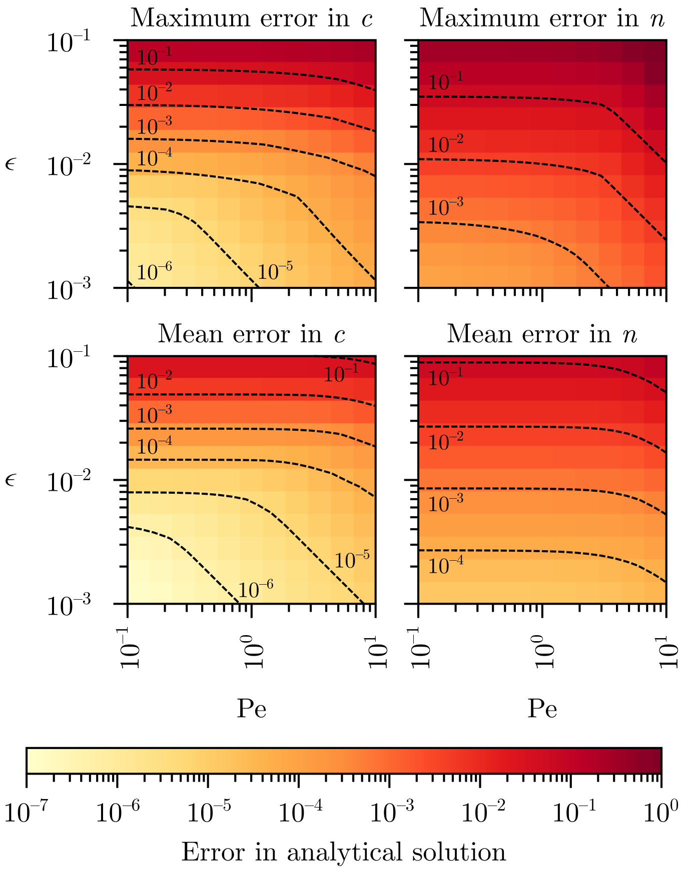

FIG. 14. The relative error associated with the analytical estimates of solute and particle concentrations, assuming numerical results are correct. The initial concentrations are given in Eq. (10). The images and contours are generated with 400 simulations with parameters ϵ and Pe equally spaced (20 values each) on a logarithmic scale and a 601 × 61 grid. The error is shown for $t^* = 0.1$ with $\Gamma_p/D_s = 1$ and $D_p/D_s = 10^{-3}$. The mean and maximum values are found by calculating the error at each point on the grid as $\frac{|c_{\text{numerical}} - c_{\text{analytical}}|}{c_{\text{numerical}}}$ and $\frac{|n_{\text{numerical}} - n_{\text{analytical}}|}{n_{\text{numerical}}}$ for solute and particles, respectively. The error in the approximate solutions increases with increasing ϵ and Pe.

in porous media and various microfluidic devices and systems. These results may provide key insights into understanding dispersions in such systems [44]. As an example extension of this work, we briefly consider how applicable these two-dimensional results are to a more general three-dimensional system in Appendix D. The numerical results show a strong focusing of particles in the corners of the channel, as seen in Fig. 16, which clearly require a fully three-dimensional treatment. Away from the the corners, however, the particle concentration resembles that predicted by our two-dimensional model, as seen in Fig. 17, which shows a comparison between the results of the two-dimensional model and the results on the midplane of the three-dimensional simulations. As can be seen, away from the channel corners, the particle dynamics in the three-dimensional channel agree well with the two-dimensional predictions.

One other limiting assumption of the current present work is our assumption that the initial conditions of the solute and particle concentrations are both functions only of x, and therefore uniform across the channel width. Thus, the precise application of the early-time solutions is limited to such cases. Furthermore, we have assumed that the fluid velocity profile is simply fully developed, pressure-driven flow. In such systems with solute concentration gradients, however, it may be expected that the channel walls would experience a diffusioosmotic effect and have a modified, transient wall-slip boundary condition, thus altering the flow profile and consequently affecting the solute and particle dynamics. We believe that the methods described herein can be extended to consider such systems, and we leave these ideas for future work.

VII. CONCLUSION

The motion of particles in a flow with a solutal concentration gradient has numerous possible applications in biological, medical, and industrial flows. Such flows often occur in narrow channels, where the effects of shear on diffusion are significant. While some researchers have studied possible applications of diffusiophoresis in microfluidic devices, most existing studies focus on the long-time behavior or require one-dimensional gradients in concentration. We show the two-dimensional dynamics of solute and particles in narrow channels. Analytical approximations capture the dynamics of each species accurately for early times, low aspect ratios ϵ, and modest Péclet numbers Pe. The approximations assume a constant particle ζ potential, and we describe how and where such an assumption can contribute as a source of error. We also extend the theoretical predictions to the long-time dynamics, and use numerical simulations to validate the theoretical predictions.

ACKNOWLEDGMENTS

This work was funded in part by the Prof. R. Bruce Lindsay Graduate Fellowship at Brown University. We thank Bhargav Rallabandi for valuable discussions about this project, including some key insights about the multiple-timescale analysis.

APPENDIX A: DETAILS OF HIGHER-ORDER SOLUTE CONCENTRATION CALCULATION

We describe the process of finding the solute concentration term c_2, necessary in Sec. II C, here. The concentration has the form $c_2 = \frac{d^2c_0}{dx^{*2}}G(y^*, t^*)$. We solve for G to obtain a solution for the solute concentration to $\mathcal{O}(\epsilon^2)$. First, we express the forcing term $(1 - \mathrm{Pe}\, u^* F)$ as a cosine series, noting

$$u^*F(y^*, t^*) = \sum_{\lambda=1}^{\infty} a_\lambda(t^*)\cos(2\lambda\pi y^*)\left(\frac{1}{2} - 6y^{*2}\right). \tag{A1}$$

The terms dependent on y^* can be written as a separate cosine series,

$$\cos(2\lambda\pi y^*)\left(\frac{1}{2} - 6y^{*2}\right) = \sum_{\theta=0}^{\infty} A_{\lambda\theta}\cos 2\theta\pi y^*.$$

The coefficients of this series are given by

$$A_{\lambda\theta} = \begin{cases} \frac{-3(-1)^\lambda}{\lambda^2\pi^2}, & \text{if } \theta = 0, \\ \frac{-3}{4\lambda^2\pi^2}, & \text{if } \theta = \lambda, \\ \frac{-6(\theta^2+\lambda^2)}{(\theta^2-\lambda^2)^2\pi^2}(-1)^{\theta+\lambda}, & \text{otherwise.} \end{cases}$$

Equation (A1) can then be simplified as

$$u^*F(y^*, t^*) = \sum_{\lambda=1}^{\infty} a_\lambda(t^*)A_{\lambda 0} + \sum_{\theta=1}^{\infty}\cos 2\theta\pi y^* \sum_{\lambda=1}^{\infty} a_\lambda(t^*)A_{\lambda\theta}. \tag{A2}$$

Substituting Eq. (A2) into Eq. (12) yields

$$\frac{\partial G}{\partial t^*} = \frac{\partial^2 G}{\partial y^{*2}} + 1 - \mathrm{Pe}\left[\sum_{\lambda=1}^{\infty} a_\lambda(t^*)A_{\lambda 0} + \sum_{\theta=1}^{\infty} \cos 2\theta\pi y^* \sum_{\lambda=1}^{\infty} a_\lambda(t^*)A_{\lambda\theta}\right].$$

We assume a solution of the form

$$G(y^*, t^*) = \sum_{\theta=0}^{\infty} b_\theta(t^*) \cos 2\theta\pi y^*.$$

For $\theta = 0$, this yields

$$b_0(t^*) = \kappa_1 + (t^* - 1) - \mathrm{Pe}\sum_{\lambda=1}^{\infty} A_{\lambda 0} I_\lambda^*(t^*),$$

where

$$I_\lambda^*(t^*) = \frac{3(-1)^\lambda \mathrm{Pe}}{8\lambda^6\pi^6}[-\exp(-4\lambda^2\pi^2) + \exp(-4\lambda^2\pi^2 t^*) + 4\lambda^2\pi^2(t^* - 1)].$$

Note that $b_\theta(0) = 0$. For $\theta \geqslant 1$, we then have

$$b_\theta'(t^*) = -4\theta^2\pi^2 b_\theta(t^*) - \mathrm{Pe}\sum_{\lambda=1}^{\infty} a_\lambda(t^*)A_{\lambda\theta}.$$

This has solution

$$b_\theta(t^*) = \sum_{\lambda=1}^{\infty} I_{\lambda\theta}(t^*) + \kappa_2 \exp(-4\theta^2\pi^2 t^*),$$

for which

$$I_{\lambda\theta} = \begin{cases} \frac{3(-1)^\lambda \mathrm{Pe}^2 A_{\lambda\theta}}{8\lambda^4\pi^6}\left[-\frac{1}{\theta^2} + \frac{\exp(-4\lambda^2\pi^2 t^*)}{\theta^2-\lambda^2}\right], & \text{if } \theta \neq \lambda, \\ \frac{-3(-1)^\lambda \mathrm{Pe}^2 A_{\lambda\lambda}}{2\lambda^4\pi^4}\left[\frac{1}{4\lambda^2\pi^2} - t^* \exp(-4\pi^2\lambda^2 t^*)\right], & \text{if } \theta = \lambda. \end{cases}$$

With $b_\theta(0) = 0$, this yields

$$\kappa_2 = -\sum_{\lambda=1}^{\infty} I_{\lambda\theta}(0),$$

which provides enough information to calculate G.

APPENDIX B: DETAILS OF LONG-TIME CONCENTRATION CALCULATIONS

This section provides the details of the calculation of solute and particle concentrations for the multiple-timescale approach described in Sec. IV.

1. Long-time solute concentration calculations

At $\mathcal{O}(\epsilon^0)$, the governing equation for the solute concentration is

$$\frac{\partial c_0}{\partial t^*} = \frac{\partial^2 c_0}{\partial y^{*2}},$$

with $c_0(t^* = 0, T^* = 0) = c_{\mathrm{init}}(x^*)$ and $\frac{\partial c_0}{\partial y^*}(y^* = \pm 1/2) = 0$. This requires $c_0(x^*, y^*, t^*, T^*) = c_0(x^*, T^*)$ and $c_0(T^* = 0) = c_{\mathrm{init}}(x^*)$.

At $\mathcal{O}(\epsilon^2)$, the governing equation is

$$\frac{\partial c_0}{\partial T^*} + \frac{\partial c_1}{\partial t^*} + \mathrm{Pe}_L\, u^* \frac{\partial c_0}{\partial x^*} = \frac{\partial^2 c_0}{\partial x^{*2}} + \frac{\partial^2 c_1}{\partial y^{*2}}. \tag{B1}$$

To isolate c_0, we average this equation across the channel and assume that the average of c_1 vanishes, such that $\langle c_1 \rangle = 0$. We check this assumption later. Note that the average of $\mathrm{Pe}_L\, u^* \frac{\partial c_0}{\partial x^*}$ across the channel is 0 because the nondimensional velocity profile u^*, given in Eq. (4), has a mean value of 0. Therefore, we have

$$\frac{\partial c_0}{\partial T^*} = \frac{\partial^2 c_0}{\partial x^{*2}} \quad \text{with} \quad c_0(T^* = 0) = c_{\mathrm{init}}(x^*).$$

To make analytical progress, we select an initial condition $c_{\mathrm{init}}(x^*) = \exp(-x^{*2})$. This is similar to the initial concentration we selected in Sec. II, though it is simpler to facilitate calculations. Here, we follow a slightly different approach and consider an infinite domain $-\infty < x < \infty$, where the characteristic length scale L is defined by the initial Gaussian solute distribution (it is, in effect, its width) rather than the length of the finite domain as before. The solution for c_0 is then given by

$$c_0(x^*, T^*) = \frac{1}{\sqrt{1 + 4T^*}} \exp\left(-\frac{x^{*2}}{1 + 4T^*}\right),$$

which is similar to results given by Chu *et al.* [20]. Then, substituting back into Eq. (B1), we have

$$\frac{\partial c_1}{\partial t^*} + \mathrm{Pe}_L\, u^* \frac{\partial c_0}{\partial x^*} = \frac{\partial^2 c_1}{\partial y^{*2}}, \tag{B2}$$

subject to the initial condition $c_1(t^* = T^* = 0) = 0$. To solve this, we note that at long times the time derivative is not important and find

$$c_1(t^* \to \infty) \sim c_1^\infty(x^*, y^*, T^*) = A(x^*, t^*, T^*) + \frac{1}{2}\mathrm{Pe}_L\left(\frac{y^{*2}}{2} - y^{*4}\right)\frac{\partial c_0}{\partial x^*},$$

where $A(x^*, t^*, T^*)$ is a constant of integration. We assumed that $\langle c_1 \rangle = 0$, so for consistency we find that $A(x^*, t^*, T^*) = -\frac{7}{480}\mathrm{Pe}_L \frac{\partial c_0}{\partial x^*}$. Therefore, we have

$$c_1^\infty(x^*, y^*, T^*) = -\frac{1}{480}\, \mathrm{Pe}_L\, (7 - 120y^{*2} + 240y^{*4})\frac{\partial c_0}{\partial x^*}.$$

Note that c_1^∞ only depends on the slow time T^*. This does not satisfy the initial condition, so it is not the full solution. We consider an additional term $\hat{c}_1$ and look for a solution $c_1(x^*, y^*, t^*, T^*) = c_1^\infty(x^*, y^*, T^*) + \hat{c}_1(x^*, y^*, t^*, T^*)$. Substituting this new form into Eq. (B2) yields

$$\frac{\partial \hat{c}_1}{\partial t^*} = \frac{\partial^2 \hat{c}_1}{\partial y^{*2}},$$

with the initial condition $\hat{c}_1(t^* = 0) = -c_1^\infty(T^* = 0)$; the solution to this is

$$\hat{c}_1 = -\mathrm{Pe}_L \left.\frac{\partial c_0}{\partial x^*}\right|_{T^*=0} \sum_{\lambda=1}^{\infty} \frac{3(-1)^\lambda}{2\lambda^4\pi^4} \exp[-(2\lambda\pi)^2 t^*] \cos(2\lambda\pi y^*).$$

We can then construct a composite solution $c_1 = c_1^\infty + \hat{c}_1$ valid for all t^*, where

$$c_1 = \mathrm{Pe}_L \frac{\partial c_0}{\partial x^*}\left[-\frac{1}{480}(7 - 120y^{*2} + 240y^{*4}) - \sum_{\lambda=1}^{\infty} \frac{3(-1)^\lambda}{2\lambda^4\pi^4} \exp[-(2\lambda\pi)^2 t^*] \cos(2\lambda\pi y^*)\right].$$

2. Long-time particle concentration calculations

At $\mathcal{O}(\epsilon^0)$, the governing equation for the particle concentration is

$$\frac{\partial n_0}{\partial t^*} = \frac{D_p}{D_s}\frac{\partial^2 n_0}{\partial y^{*2}},$$

with $n_0(t^* = 0, T^* = 0) = n_{\text{init}}(x^*)$ and $\frac{\partial n_0}{\partial y^*}(y^* = \pm 1/2) = 0$. This requires, as with the solute, that $n_0(x^*, y^*, t^*, T^*) = n_0(x^*, T^*)$ and $n_0(T^* = 0) = n_{\text{init}}(x^*)$.

At $\mathcal{O}(\epsilon^2)$, we have

$$\begin{aligned}\frac{\partial n_0}{\partial T^*} = \frac{D_p}{D_s}\frac{\partial^2 n_0}{\partial x^{*2}} + \frac{\Gamma_p}{D_s}\left[\frac{n_0}{c_0^2}\left(\frac{\partial c_0}{\partial x^*}\right)^2 - \frac{1}{c_0}\frac{\partial c_0}{\partial x^*}\frac{\partial n_0}{\partial x^*} - \frac{n_0}{c_0}\frac{\partial^2 c_0}{\partial x^{*2}} - \frac{n_0}{c_0}\frac{\partial^2 c_1}{\partial y^2}\right]\\ - \text{Pe}_L\, u^*\frac{\partial n_0}{\partial x^*} - \frac{\partial n_1}{\partial t^*} + \frac{D_p}{D_s}\frac{\partial^2 n_1}{\partial y^{*2}}.\end{aligned} \tag{B3}$$

As before, to isolate n_0, we average this equation across the channel and assume that $\langle n_1\rangle = 0$, which we enforce later. This gives

$$\frac{\partial n_0}{\partial T^*} = \frac{\Gamma_p}{D_s}\left[\frac{n_0}{c_0^2}\left(\frac{\partial c_0}{\partial x^*}\right)^2 - \frac{1}{c_0}\frac{\partial c_0}{\partial x^*}\frac{\partial n_0}{\partial x^*} - \frac{n_0}{c_0}\frac{\partial^2 c_0}{\partial x^{*2}}\right] + \frac{D_p}{D_s}\frac{\partial^2 n_0}{\partial x^{*2}}. \tag{B4}$$

Substituting the form for $c_0(x^*, T^*)$ from Appendix B 1 and again utilizing a simple Gaussian initial condition $n_{\text{init}}(x^*) = \exp(-x^{*2})$, we have

$$\frac{\partial n_0}{\partial T^*} = \frac{2}{1+4T^*}\frac{\Gamma_p}{D_s}\left(n_0 + x^*\frac{\partial n_0}{\partial x^*}\right) + \frac{D_p}{D_s}\frac{\partial^2 n_0}{\partial x^{*2}}. \tag{B5}$$

Following the work of Chu *et al.* [20], we can find the solution to Eq. (B5). We first define a function

$$B(T^*) = 1 + \frac{\Gamma_p}{D_s} + \frac{D_p}{D_s}\left[-1 + (1+4T^*)^{1+\frac{\Gamma_p}{D_s}}\right]$$

for convenience and subsequently find the solution

$$n_0(x^*, T^*) = \frac{\exp\left[-[B(T^*)]^{-1}\left(1+\frac{\Gamma_p}{D_s}\right)(1+4T^*)^{\frac{\Gamma_p}{D_s}}x^{*2}\right]}{\sqrt{B(T^*)(1+4T^*)^{-\frac{\Gamma_p}{D_s}}\left(1+\frac{\Gamma_p}{D_s}\right)^{-1}}}.$$

Substituting Eq. (B4) back into Eq. (B3), we have

$$\frac{\Gamma_p}{D_s}n_0\frac{\partial^2 c_1}{\partial y^{*2}} + c_0\left(\text{Pe}_L\, u^*\frac{\partial n_0}{\partial x^*} + \frac{\partial n_1}{\partial t^*} - \frac{D_p}{D_s}\frac{\partial^2 n_1}{\partial y^{*2}}\right) = 0. \tag{B6}$$

Again, we first seek the solution at long times, so that $\frac{\partial n_1}{\partial t^*}$ is negligible. This gives

$$n_1(t^* \to \infty) \sim n_1^\infty(x^*, y^*, T^*) = -\frac{\text{Pe}_L}{480}\frac{D_s}{D_p}\frac{1}{c_0}(7 - 120y^{*2} + 240y^{*4})\left(\frac{\Gamma_p}{D_s}n_0\frac{\partial c_0}{\partial x^*} + c_0\frac{\partial n_0}{\partial x^*}\right).$$

We now look for a solution $n_1(x^*, y^*, t^*, T^*) = n_1^\infty(x^*, y^*, T^*) + \hat{n}_1(x^*, y^*, t^*, T^*)$, which we substitute into Eq. (B6) to find

$$\frac{\partial \hat{n}_1}{\partial t^*} + \frac{\Gamma_p}{D_s}\frac{n_0}{c_0}\frac{\partial^2 \hat{c}_1}{\partial y^{*2}} = \frac{D_p}{D_s}\frac{\partial^2 \hat{n}_1}{\partial y^{*2}}.$$

Following the form of $\hat{c}_1$ in Appendix B 1, we assume a form for $\hat{n}_1$ given by

$$\hat{n}_1 = \sum_{\lambda=1}^{\infty} a_\lambda(x^*, T^*)\exp[-(2\lambda\pi)^2 t^*]\cos(2\lambda\pi y^*).$$

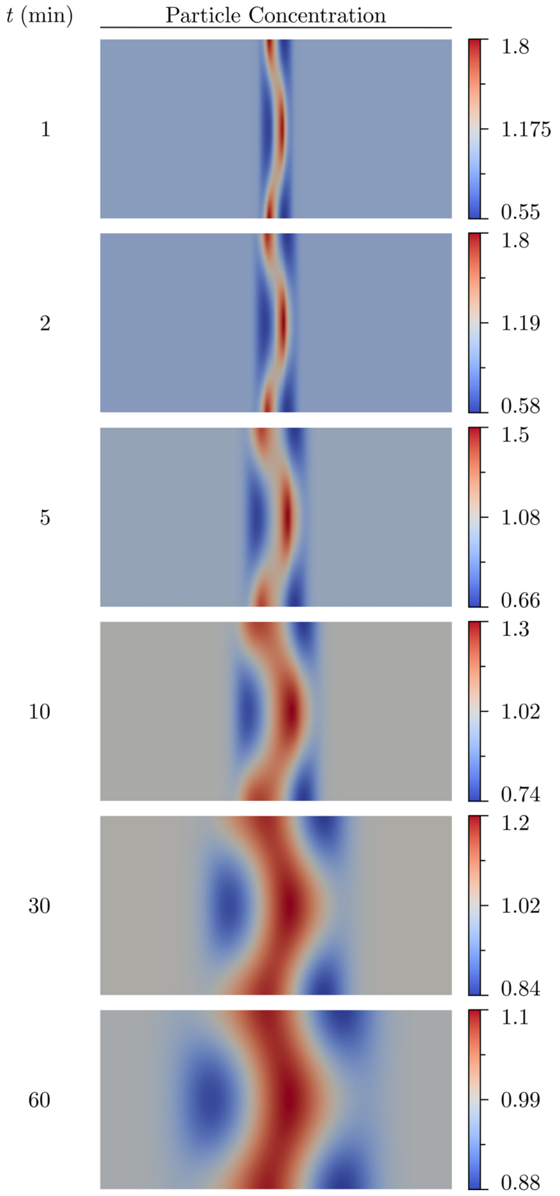

FIG. 15. A sample of the evolution of the particle concentration profile over a period of 1 h, based on simulations in OpenFOAM. The channel is 50 μm × 34 mm (to ensure the changes in concentration near the inlet and outlet are negligible). The kinematic viscosity is $\nu = 1 \times 10^{-6}\,\mathrm{m^2\,s^{-1}}$. The diffusivity values are $D_s = 1.6 \times 10^{-9}\,\mathrm{m^2\,s^{-1}}$ (corresponding to NaCl in water) and $D_p = 1.07 \times 10^{-12}\,\mathrm{m^2\,s^{-1}}$ (corresponding to 200 nm particles at 293 K with $\mu = 10^{-3}$). The diffusiophoretic mobility is taken to be $\Gamma_p = D_s/2 = 8 \times 10^{-10}\,\mathrm{m^2\,s^{-1}}$. The initial salt concentration is given by $c_0 = (1 - 0.01)\exp[-\frac{1}{2}(\frac{x}{0.05 \cdot 5 \times 10^{-3}})^2] + 0.01$. The velocity profile is parabolic with a mean velocity of $10^{-6}\,\mathrm{m\,s^{-1}}$. The particle distribution is two-dimensional, even after an hour, in part due to the relatively low particle diffusivity.

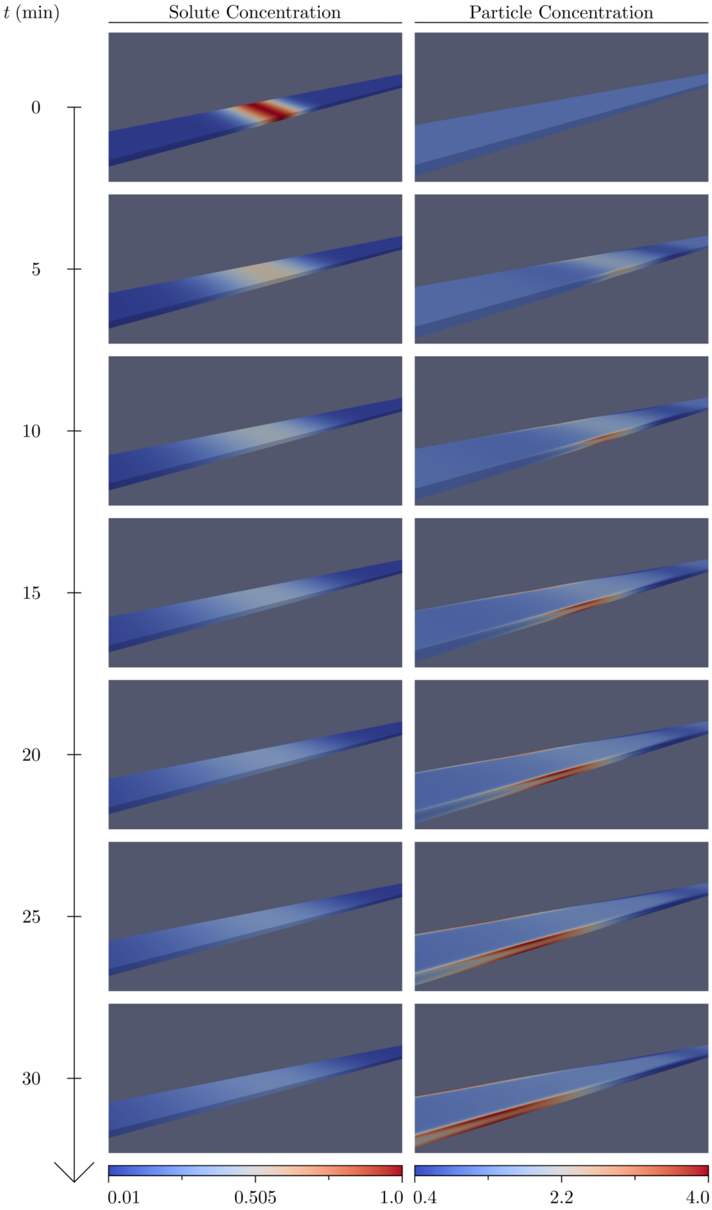

FIG. 16. An illustration of the evolution of solute and particle concentration profiles in a three-dimensional channel, based on simulations in OpenFOAM. The channel is $50\,\mu$m $\times$ $500\,\mu$m $\times$ 34 mm. The kinematic viscosity is $\nu = 1 \times 10^{-6}\,\mathrm{m^2\,s^{-1}}$. The diffusivity values are $D_s = 1.6 \times 10^{-9}\,\mathrm{m^2\,s^{-1}}$ (corresponding to NaCl in water) and $D_p = 1.07 \times 10^{-12}\,\mathrm{m^2\,s^{-1}}$ (corresponding to 200 nm particles at 293 K with $\mu = 1 \times 10^{-3}$ Pa s). The diffusiophoretic mobility is taken to be $\Gamma_p = D_s/2 = 8 \times 10^{-10}\,\mathrm{m^2\,s^{-1}}$. The initial salt concentration is given by $c_0 = (1 - 0.01)\exp[-\frac{1}{2}(\frac{x}{0.05 \cdot 5 \times 10^{-3}})^2] + 0.01$. The velocity profile is parabolic with a mean velocity of $1 \times 10^{-6}\,\mathrm{m\,s^{-1}}$. A key distinction between the two- and three-dimensional results is the enhanced particle focusing at the corners of the channel.

Substituting into the governing equation, we find that

$$a_\lambda(x^*, T^*) = -\frac{3(-1)^\lambda}{2\lambda^4\pi^4}\mathrm{Pe}_L \frac{n_0}{c_0}\frac{\partial c_0}{\partial x^*}\frac{\Gamma_p/D_s}{D_p/D_s - 1}.$$

However, we have not yet satisfied the initial condition that $n_1(t^* = T^* = 0) = 0$, so we further extend the analysis to consider a solution $n_1(x^*, y^*, t^*, T^*) = n_1^\infty(x^*, y^*, T^*) + \hat{n}_1(x^*, y^*, t^*, T^*) + \tilde{n}_1(x^*, y^*, t^*, T^*)$, where $\tilde{n}_1$ satisfies

$$\frac{\partial \tilde{n}_1}{\partial t^*} = \frac{D_p}{D_s}\frac{\partial^2 \tilde{n}_1}{\partial y^{*2}},$$

with $\tilde{n}_1(t^* = T^* = 0) = -n_1^\infty(T^* = 0) - \hat{n}_1(t^* = T^* = 0)$. This has the solution

$$\tilde{n}_1(x^*, y^*, t^*, T^*) = \sum_{\lambda=1}^{\infty} \frac{3(-1)^\lambda D_s\,\mathrm{Pe}_L}{2D_p(D_p - D_s)\lambda^4\pi^4}\left[\Gamma_p \frac{n_0}{c_0}\frac{\partial c_0}{\partial x^*} + (D_s - D_p)\frac{\partial n_0}{\partial x^*}\right]$$
$$\times \exp\left[\frac{-(2\lambda\pi)^2 t^* D_p}{D_s}\right]\cos(2\lambda\pi y^*).$$

Finally, we can combine the earlier results and find a solution

$$n(x^*, y^*, t^*) = n_0(x^*, t^*) + \epsilon^2\big[n_1^\infty(x^*, y^*, t^*) + \hat{n}_1(x^*, y^*, t^*) + \tilde{n}_1(x^*, y^*, t^*)\big],$$

where we have replaced every T^* with $\epsilon^2 t^*$.

3. Description of simulations

Simulations for the multiple-timescale analysis are performed with a finite volume approach that is second-order accurate in space and first-order accurate (explicit) in time. The simulations use a 200×40 grid with a time step of 2×10^{-4} dimensionless time units. Infinite sums are approximated with 50 terms.

APPENDIX C: EXAMPLE OF LONG-TIME SIMULATION

Here, we demonstrate how, for certain parameter regimes, the "early-time" dynamics can persist for what may be surprisingly long physical times. In particular, we show the persistence of two-dimensional structures in the particle distribution for a channel of width 50 μm and with particles of

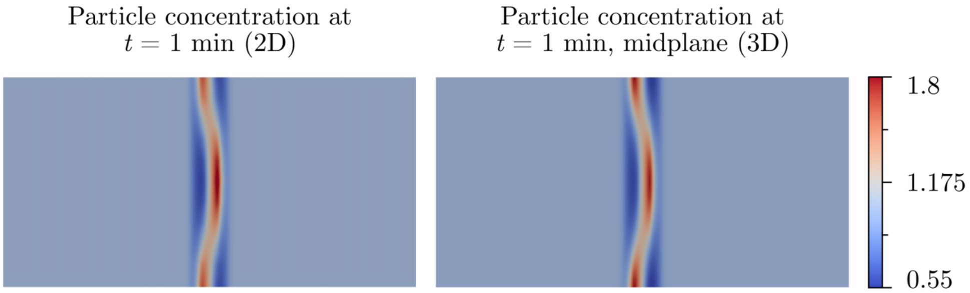

FIG. 17. A comparison of the concentration of particles from a two-dimensional simulation (see Appendix C) and at the midplane (250 μm from the side walls) of the three-dimensional channel at $t = 1$ min. The parameters in this simulation are the same as those given in Fig. 16. The simulation was performed in OpenFOAM. The profiles are qualitatively and quantitatively very similar (though there is enhanced focusing at walls in the case of the three-dimensional channel), which suggests the two-dimensional approximation is useful for regions far from side walls.

(a) Numerical estimate of solute concentration at $x^* = 0.5$

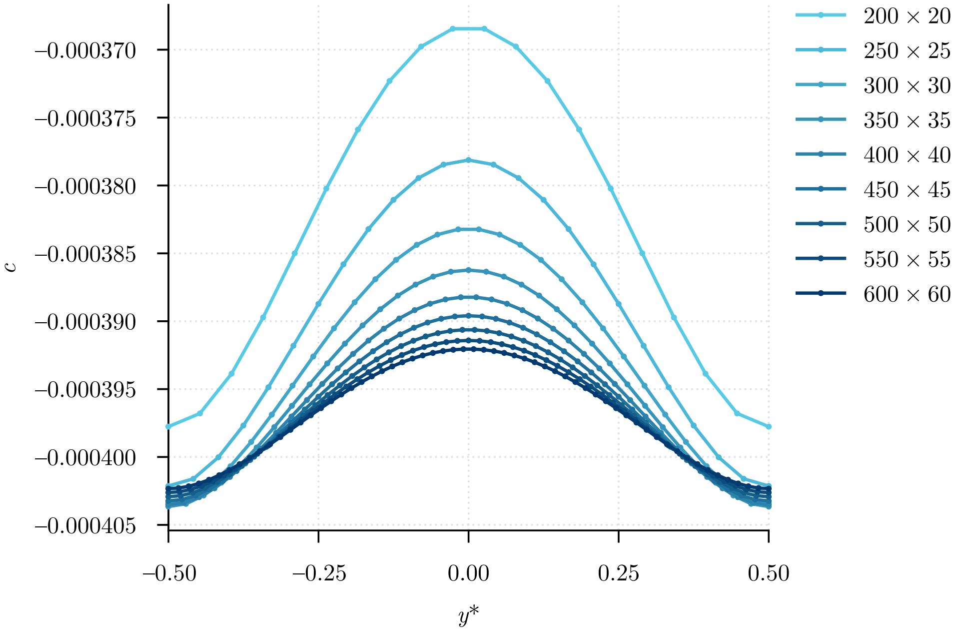

(b) Numerical estimate of particle concentration at $x^* = 0.5$

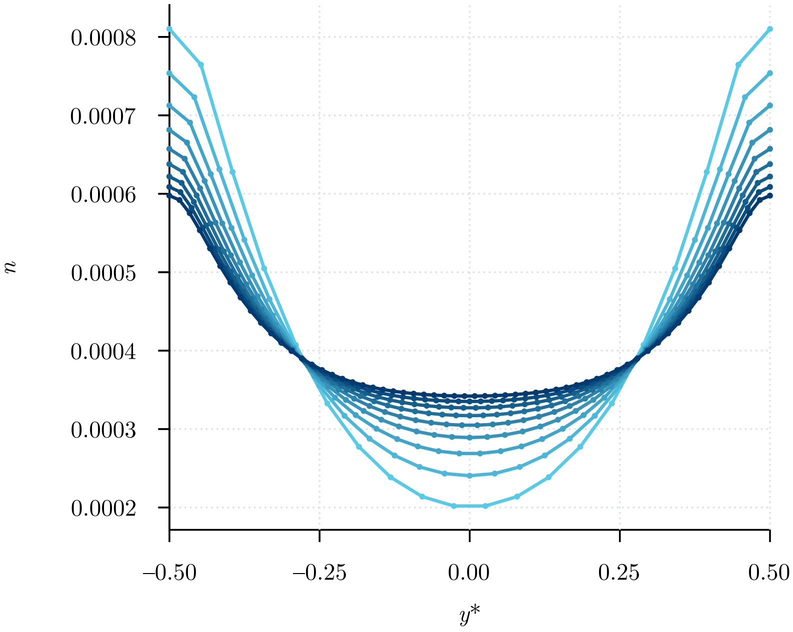

FIG. 18. A slice of concentrations at $x^* = 0.5$ for various grid resolutions at $t^* = 1$ with Pe $= 1$, $\Gamma_p/D_s = 1$, $D_p/D_s = 10^{-3}$, and $\epsilon = 10^{-3}$. The initial concentrations are given in Eq. (10). The concentration of each species changes slowly near the grid resolution we employ, which suggests the results have converged.

size 200 nm in Fig. 15. Here, the simulation represents a total duration of one hour in physical time, after which the particle distribution still shows clear two-dimensional structures after a simulated time period of one hour.

APPENDIX D: THREE-DIMENSIONAL SIMULATION

Here, we present a brief comparison of the two-dimensional predictions with the results of fully three-dimensional numerical simulations. In particular, three-dimensional numerical simulation results for the solute and particle concentrations are presented in Fig. 16. One key change of the introduction of three-dimensional effects is the enhanced particle focusing that occurs at the corners of the channel. In regions near the corners, the two-dimensional predictions breakdown due to the fully three-dimensional nature of the flow. However, away from the corners, we find that the particle concentration still agrees well with the predictions of the two-dimensional theory of Secs. II and III. This is illustrated in Fig. 17, which shows a comparison of the two-dimensional results with the particle concentration profile taken from the midplane of the three-dimensional channel results.

APPENDIX E: CONVERGENCE STUDY

To demonstrate that the numerical solutions from Sec. III have converged, we plot values of the concentrations of solute and particles across the channel at $x^* = 0.5$ and $t^* = 1$ (the largest time considered in Fig. 12). The results are shown in Fig. 18. Here, there is little variation between grids of size 550×55 and 600×60, and thus for the purposes of validating the theoretical predictions, we determine that the 600×60 grid is sufficiently well refined. We also plot the relative error in

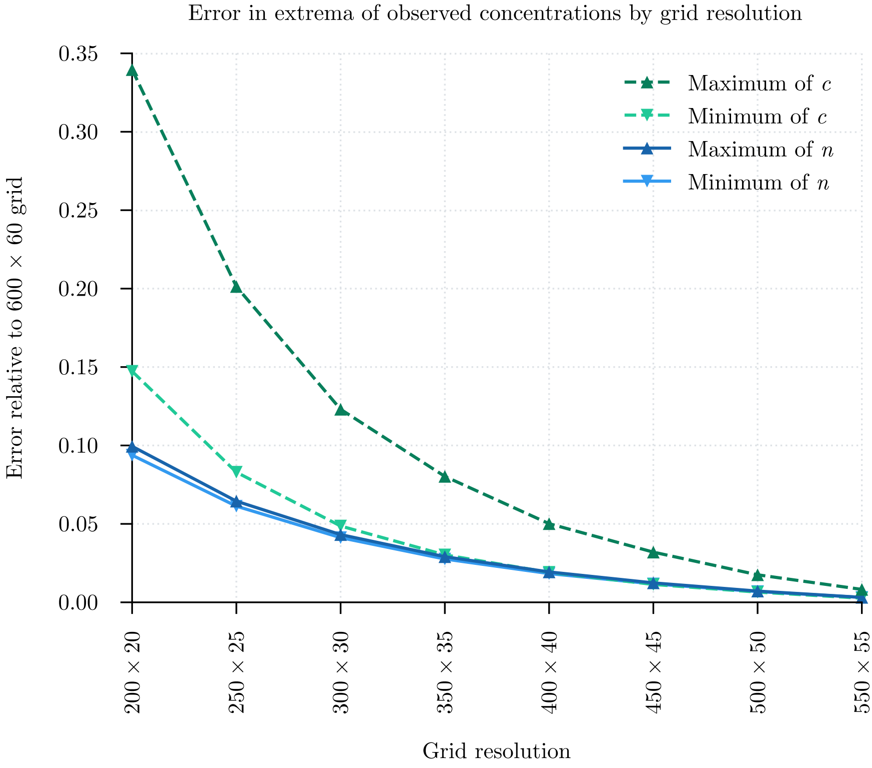

FIG. 19. Error in extrema of c and n at $t^* = 1$ with $\mathrm{Pe} = 1$, $\Gamma_p/D_s = 1$, $D_p/D_s = 10^{-3}$, and $\epsilon = 10^{-3}$. The initial concentrations are given in Eq. (10). The error is calculated as $\frac{|c_{\text{numerical}} - c_{\text{analytical}}|}{c_{\text{numerical}}}$ and $\frac{|n_{\text{numerical}} - n_{\text{analytical}}|}{n_{\text{numerical}}}$ for solute and particles, respectively. The decay in error illustrates the convergence as the grid is refined.

the extrema of c and n, using the solution with the 600×60 grid as the baseline. These results are shown in Fig. 19. The error appears to decrease with increasing resolution, as in Fig. 18.

[1] G. I. Taylor, Dispersion of soluble matter in solvent flowing slowly through a tube, Proc. R. Soc. London A **219**, 186 (1953).

[2] J. L. Anderson and D. C. Prieve, Diffusiophoresis: Migration of colloidal particles in gradients of solute concentration, Sep. Purif. Methods **13**, 67 (1984).

[3] S. Shin, E. Um, B. Sabass, J. T. Ault, M. Rahimi, P. B. Warren, and H. A. Stone, Size-dependent control of colloid transport via solute gradients in dead-end channels, Proc. Natl. Acad. Sci. USA **113**, 257 (2016).

[4] B. V. Derjaguin, G. P. Sidorenkov, E. A. Zubashchenkov, and E. V. Kiseleva, Kinetic phenomena in boundary films of liquids, Kolloidn. Zh. **9**, 335 (1947).

[5] B. V. Derjaguin, S. S. Dukhin, and A. Korotkova, Adhesion of powder particles to plane surfaces, Kolloidn. Zh. **23**, 53 (1961).

[6] J. L. Anderson, Colloid transport by interfacial forces, Annu. Rev. Fluid Mech. **21**, 61 (1989).

[7] M. M. J. Lin and D. C. Prieve, Electromigration of latex induced by a salt gradient, J. Colloid Interface Sci. **95**, 327 (1983).

[8] W. J. Lechnick and J. A. Shaeiwitz, Measurement of diffusiophoresis in liquids, J. Colloid Interface Sci. **102**, 71 (1984).

[9] P. O. Staffeld and J. A. Quinn, Diffusion-induced banding of colloid particles via diffusiophoresis, J. Colloid Interface Sci. **130**, 69 (1989).

[10] S. Shin, J. T. Ault, P. B. Warren, and H. A. Stone, Accumulation of Colloidal Particles in Flow Junctions Induced by Fluid Flow and Diffusiophoresis, Phys. Rev. X **7**, 041038 (2017).

[11] A. Kar, T.-Y. Chiang, I. O. Rivera, A. Sen, and D. Velegol, Enhanced transport into and out of dead-end pores, ACS Nano **9**, 746 (2015).

[12] S. Shin, P. B. Warren, and H. A. Stone, Cleaning by Surfactant Gradients: Particulate Removal from Porous Materials and the Significance of Rinsing in Laundry Detergency, Phys. Rev. Appl. **9**, 034012 (2018).

[13] S. Shim and H. A. Stone, CO_2-leakage-driven diffusiophoresis causes spontaneous accumulation of charged materials in channel flow, Proc. Natl. Acad. Sci. USA **117**, 25985 (2020).

[14] S. Shim, S. Khodaparast, C.-Y. Lai, J. Yan, J. T. Ault, B. Rallabandi, O. Shardt, and H. A. Stone, CO_2-driven diffusiophoresis for maintaining a bacteria-free surface, Soft Matter **17**, 2568 (2021).

[15] D. Florea, S. Musa, J. M. R. Huyghe, and H. M. Wyss, Long-range repulsion of colloids driven by ion exchange and diffusiophoresis, Proc. Natl. Acad. Sci. USA **111**, 6554 (2014).

[16] D. C. Elton, P. D. Spencer, J. D. Riches, and E. D. Williams, Exclusion zone phenomena in water—a critical review of experimental findings and theories, Int. J. Mol. Sci. **21**, 5041 (2020).

[17] Y.-F. Lee, W.-C. Chang, Y. Wu, L. Fan, and E. Lee, Diffusiophoresis of a highly charged soft particle in electrolyte solutions, Langmuir **37**, 1480 (2021).

[18] F. Raynal, M. Bourgoin, C. Cottin-Bizonne, C. Ybert, and R. Volk, Advection and diffusion in a chemically induced compressible flow, J. Fluid Mech. **847**, 228 (2018).

[19] J. T. Ault, P. B. Warren, S. Shin, and H. A. Stone, Diffusiophoresis in one-dimensional solute gradients, Soft Matter **13**, 9015 (2017).

[20] H. C. W. Chu, S. Garoff, R. D. Tilton, and A. S. Khair, Advective-diffusive spreading of diffusiophoretic colloids under transient solute gradients, Soft Matter **16**, 238 (2020).

[21] H. C. Chu, S. Garoff, R. D. Tilton, and A. S. Khair, Macrotransport theory for diffusiophoretic colloids and chemotactic microorganisms, J. Fluid Mech. **917**, A52 (2021).

[22] J. T. Ault, S. Shin, and H. A. Stone, Diffusiophoresis in narrow channel flows, J. Fluid Mech. **854**, 420 (2018).

[23] J. T. Ault, S. Shin, and H. A. Stone, Characterization of surface–solute interactions by diffusioosmosis, Soft Matter **15**, 1582 (2019).

[24] M. K. Rasmussen, J. N. Pedersen, and R. Marie, Size and surface charge characterization of nanoparticles with a salt gradient, Nat. Commun. **11**, 2337 (2020).

[25] N. Shi, R. Nery-Azevedo, A. I. Abdel-Fattah, and T. M. Squires, Diffusiophoretic Focusing of Suspended Colloids, Phys. Rev. Lett. **117**, 258001 (2016).

[26] B. M. Alessio, S. Shim, E. Mintah, A. Gupta, and H. A. Stone, Diffusiophoresis and diffusioosmosis in tandem: Two-dimensional particle motion in the presence of multiple electrolytes, Phys. Rev. Fluids **6**, 054201 (2021).

[27] D. Velegol, A. Garg, R. Guha, A. Kar, and M. Kumar, Origins of concentration gradients for diffusiophoresis, Soft Matter **12**, 4686 (2016).

[28] R. Aris, On the dispersion of a solute in a fluid flowing through a tube, Proc. R. Soc. London A **235**, 67 (1956).

[29] I. Frankel and H. Brenner, On the foundations of generalized Taylor dispersion theory, J. Fluid Mech. **204**, 97 (1989).

[30] N. G. Barton, On the method of moments for solute dispersion, J. Fluid Mech. **126**, 205 (1983).

[31] H. C. W. Chu, S. Garoff, T. M. Przybycien, R. D. Tilton, and A. S. Khair, Dispersion in steady and time-oscillatory two-dimensional flows through a parallel-plate channel, Phys. Fluids **31**, 022007 (2019).

[32] H. R. Bailey and W. B. Gogarty, Numerical and experimental results on the dispersion of a solute in a fluid in laminar flow through a tube, Proc. R. Soc. London A **269**, 352 (1962).

[33] L. G. Leal, *Advanced Transport Phenomena: Fluid Mechanics and Convective Transport Processes* (Cambridge University Press, Cambridge, UK, 2007)

[34] B. J. Kirby and E. F. Hasselbrink, Zeta potential of microfluidic substrates: 1. Theory, experimental techniques, and effects on separations, Electrophoresis **25**, 187 (2004).

[35] J. Palacci, B. Abécassis, C. Cottin-Bizonne, C. Ybert, and L. Bocquet, Colloidal Motility and Pattern Formation Under Rectified Diffusiophoresis, Phys. Rev. Lett. **104**, 138302 (2010).

[36] S. Lee, J. Lee, and J. Ault, The role of variable-zeta potential on diffusiophoretic and diffusioosmotic transport (unpublished).

[37] S. Shin, Diffusiophoretic separation of colloids in microfluidic flows, Phys. Fluids **32**, 101302 (2020).

[38] D. C. Prieve, J. L. Anderson, J. P. Ebel, and M. E. Lowell, Motion of a particle generated by chemical gradients. Part 2. Electrolytes, J. Fluid Mech. **148**, 247 (1984).

[39] B. Abécassis, C. Cottin-Bizonne, C. Ybert, A. Ajdari, and L. Bocquet, Boosting migration of large particles by solute contrasts, Nat. Mater. **7**, 785 (2008).

[40] J. Palacci, C. Cottin-Bizonne, C. Ybert, and L. Bocquet, Osmotic traps for colloids and macromolecules based on logarithmic sensing in salt taxis, Soft Matter **8**, 980 (2012).

[41] A. Banerjee, I. Williams, R. N. Azevedo, M. E. Helgeson, and T. M. Squires, Soluto-inertial phenomena: Designing long-range, long-lasting, surface-specific interactions in suspensions, Proc. Natl. Acad. Sci. USA **113**, 8612 (2016).

[42] D. G. Archer and P. Wang, The dielectric constant of water and Debye-Hückel limiting law slopes, J. Phys. Chem. Ref. Data **19**, 371 (1990).

[43] C. C. Miller, The Stokes-Einstein law for diffusion in solution, Proc. R. Soc. London A **106**, 724 (1924).

[44] D. Dutta, A. Ramachandran, and D. T. Leighton, Effect of channel geometry on solute dispersion in pressure-driven microfluidic systems, Microfluid. Nanofluid. **2**, 275 (2006).

Correction: Equation (6) and the displayed equations in Sec. II D contained the wrong sign before $\frac{\Gamma_p}{D_s}$ and have been fixed. In Figure 6, the directions of the blue curves were erroneous and have been reversed. The color indicators in the rightmost panels of Figs. 7, 12, and 13 and in both panels of Fig. 10 were presented incorrectly and have been reversed.